

Structural test and analyses of UHPC horizontal connection with shear keys for slab-external PC wall

Nguyen Huu Cuong ^a, Hyoseo An ^a, Han V. Tran ^{b,a}, Sanghee An ^c, Kihak Lee ^{a,*}

^a Deep Learning Architecture Research Center, Department of Architectural Engineering, Sejong University, 209 Neungdong-ro, Gwangjin-gu, Seoul 05006, South Korea

^b Faculty of Civil Engineering, Mien Trung University of Civil Engineering, Tuy Hoa and Danang, Viet Nam

^c JeongYang SG Co., LTD, South Korea



ARTICLE INFO

Keywords:

Structural capacity
Shear key
Heat loss
UHPC
FEM analysis

ABSTRACT

In residential buildings, the connection between the wall and the slab is the most important area for the design to prevent structural failure and heat loss. The research objective is to evaluate the load capacity of connecting shear keys to an existing slab and panel concrete (PC) wall structure, as well as to develop a design for this connection under direct shear and bending. The experimental program included four test specimens, two of which had one shear key and two shear keys for the others for each loading condition. The test results demonstrate that the structural bearing capacity of bending and shear are significantly improved by changes to the dimensions of the slab, the design of the shear key, and the number of ribs, with the ultimate load increased by 54.45% and 56.85%, respectively. In addition, a finite element (FE) model was used to numerically simulate the behavior of all specimens. The crack and load-displacement curves of the numerical simulations were validated against experimental results using the LS-DYNA program, and good agreement was observed, demonstrating the effectiveness of the numerical model for simulating the behavior of the system components. Several critical input parameters, a constitutive model, and a bar-concrete interface are recommended. The experiments and simulations highlight the effectiveness of various technical solutions for boosting the load capacity of the structure.

1. Introduction

The demand for energy has been rapidly increasing in response to continuing economic development. It has been observed that, in Korea, 43.5% of the total energy consumed in residential areas is used in apartment buildings [1]. This highlights the significant effect of apartment buildings on the overall energy consumption of the country. According to some research, up to 30% of the total consumed energy can be lost due to factors such as poorly insulated walls, windows, roofs, or connection points between components [2–6]. It is critical to ensure sufficient insulation for each building component in order to limit heat loss, especially in traditional connections in structures, which experience more heat gain in the summer and heat loss in the winter. A thermal bridge is a construction component that has significantly different thermal performance than other components, particularly in the areas where walls, floors, and ceilings connect [7]. To address the heat loss effect, numerous studies have investigated various methods of connecting, particularly those made of reinforced concrete, with a focus on reducing heat transfer through the structures by use of mechanical

systems, lighting, and building envelopes [8–13]. Modern buildings have attempted to reduce thermal bridging by utilizing curtain wall or window-wall construction technologies. However, even with these approaches, the thermal bridge at a connection has been difficult to completely eliminate.

The Korean building code has not requested a detailed thermal bridge calculation of its bearing capacity. The solution proposed in this study is presented to enhance practical research in the field of thermal bridges, as shown in Figs. 1 and 2. As can be seen, Fig. 2 depicts the new design of the connection, which is a panel concrete PC wall, slab, and ultra-high performance concrete (UHPC) ribs. In comparison to conventional concrete, UHPC ribs provide outstanding compressive strength and low thermal conductivity in building construction [14,15]. To maintain structural integrity, the UHPC precast construction method and reinforcement bars are added to reinforce the UHPC rib to perform the structural load transfer to other elements. Also, incorporating shear keys can significantly enhance the shear strength of the structure. The proposed insulation solution offers the advantage of convenient

* Corresponding author.

E-mail address: kihaklee@sejong.ac.kr (K. Lee).

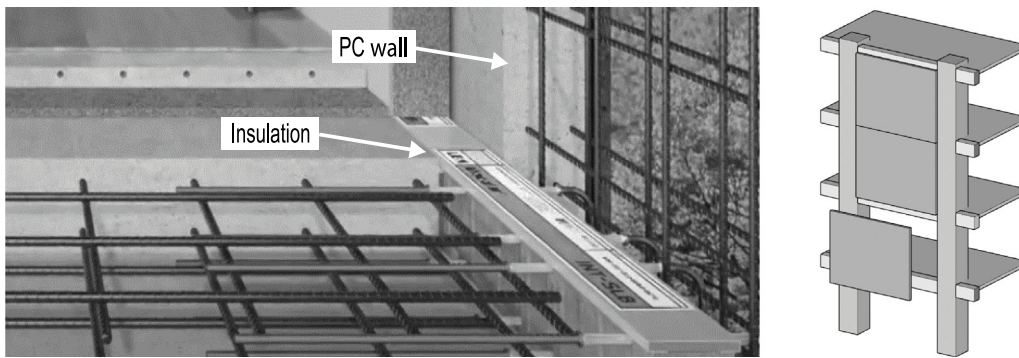


Fig. 1. Slab connection PC wall.

on-site installation following factory production, and it is specifically designed to fit at the intersection of an existing wall and slab. The utilization of UHPC minimizes the volume of the compressed block while simultaneously improving structural performance compared to normal concrete. Expanded Polystyrene (EPS) insulation is installed between the slab to reduce the structural weight of the building.

According to recent studies, LS-DYNA can simulate the behavior of concrete structures under various loading conditions, including phenomena such as concrete cracking and the effects of reinforcement. Four commonly utilized concrete constitutive models include the MAT072R3 model (KCC) [16], the MAT084/085 model (Winfirth) [17, 18], the MAT159 model (CSC) [19], and the MAT273 model (CDP). The Winfrith model can predict the mechanical behavior of concrete, including the position of cracks, with acceptable accuracy [20, 21]. A total of four specimens were built and tested under static loading conditions to investigate the behavior of the connection. The behavior of the reinforced concrete structures was simulated using numerical models. Four models were built to compare with experiment results; the Winfrith model was selected, and results obtained from the simulation demonstrated that the model could acceptably estimate crack failure and the load-displacement curve. In addition, parametric studies of the concrete strength were conducted to find the failure mode and the peak load with one and two shear keys of the UHPC rib cases.

The main novelty of this paper is to compare the effects of the two thermal bridge solutions on the slab connection with varying detailed configurations in terms of bearing capacity. Structural performance tests were carried out to determine whether the UHPC ribs could accurately represent the performance of the structure under various loading conditions. A novel design was developed, and the accuracy and robustness of the method were demonstrated by comparing the numerical model with experimental results.

Fig. 3 describes a plan to investigate and address issues with insulation performance, connection durability, the number of shear keys, and UHPC ribs in building construction. This plan involves four key steps, starting with a definition of the research objectives, followed by planning the testing procedures, collecting data through various tests, and then using computational simulation to analyze and enhance the design. The overall aim is to develop an insulation structure that is capable of a variety of loads.

This work is presented as follows: Section 1 shows the purpose of the experiment. Section 2 provides detailed information regarding the results of the experiment. Section 3 discusses these results, which are validated using the numerical model LS-DYNA in Sections 4 and 5. In Section 6, the effects of the strength of concrete and rebar are investigated. Then, some conclusions are summarized in Section 7.

2. Experimental investigation

2.1. Material properties

The Portland cement used in the study was of the Class 1 Normal type and had a surface area ranging from 0.28 to 0.34 m²/g and a

Table 1
Mix proportion of UHPC (Unit: kg/m³).

Materials	Cement	Silica	Sand	Silica powder	Steel fiber	Water
UHPC	830	220	500	280	75	190

density of 830 kg/m³. The silica fume used had a specific surface area of 15 to 35 m²/g and a density of 220 kg/m³. Table 1 presents the details of the UHPC mixture proportions. As shown in Fig. 2, the core of the separator is comprised of high-quality insulating material of 150 mm and 210 mm thickness expanded polystyrene, with insulation spacing of 150 mm and 200 mm, respectively. Expanded polystyrene has a Poisson's ratio of 0.3, a compressive strength of 0.27 MPa and a mass density of 3 kg/m³, respectively.

The compressive strength of the UHPC specimen was evaluated by conducting compression tests on cube-shaped specimens with dimensions of 100 × 100 × 100 mm³ [22–24]. The tests were carried out according to ASTM C1856 and ASTM C39 standards, and at least three specimens were tested. Similarly, the compressive strength of standard concrete was determined by subjecting three cylinder-shaped specimens with 150 mm diameters and 300 mm heights to uniaxial compression tests using a universal testing machine with a capacity of 2000 kN. To ensure an even distribution of load, two neoprene pads were inserted between the steel plates and the specimens. Two separate specimen types were used, which vary depending on laboratory conditions and equipment. The average compressive strength of concrete in all the specimens was consistent, with an average of 27 MPa for normal concrete and 160 MPa for the UHPC specimens. The average yield strength f_y of reinforcement for D13 was recorded to be 502 MPa. The parameters of the UHPC concrete and conventional concrete materials were reported in previous work [25].

2.2. Specimen design and construction

The experimental program involved four test specimens, which were divided into two groups: two specimens had four UHPC ribs and one shear key, while the other two had five UHPC ribs and two shear keys. These specimens were tested under static loading bending and shear tests, as listed in Table 2.

Four specimens with thicknesses of 150 mm and 210 mm were constructed to verify the structural performance of the horizontal UHPC connection. Structural performance testing was conducted by applying vertical loads to these specimens. The bending and shear performance of the UHPC horizontal connection system were investigated by varying the position of the vertical load. To ensure safety during the shear test, one end of the test specimen was hinged, while the other end acted as a support point. For the bending test, the test specimen was subjected to cantilever conditions without any support at the end, as depicted in Fig. 7. The diameter of the reinforcement, the type of material used for the UHPC, and the heating procedure for the samples were all kept

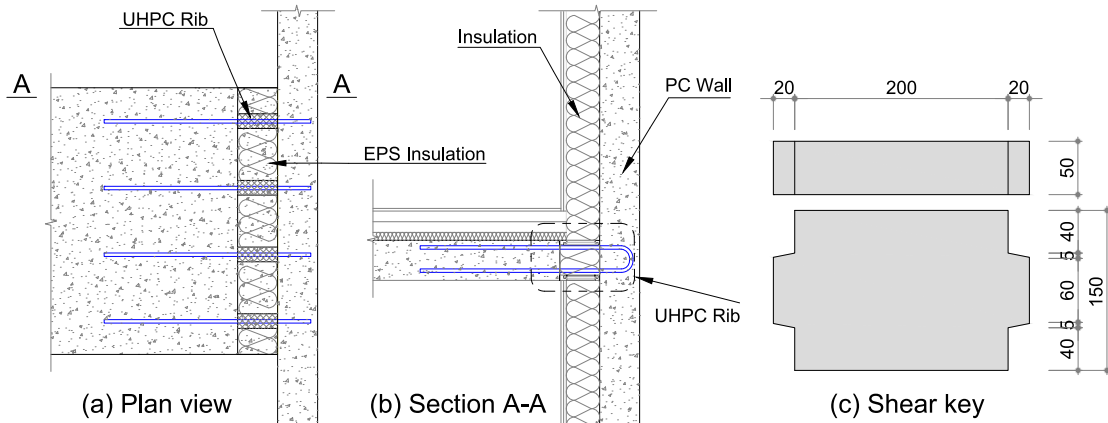


Fig. 2. Shape and composition of the horizontal UHPC thermal insulation ribs.

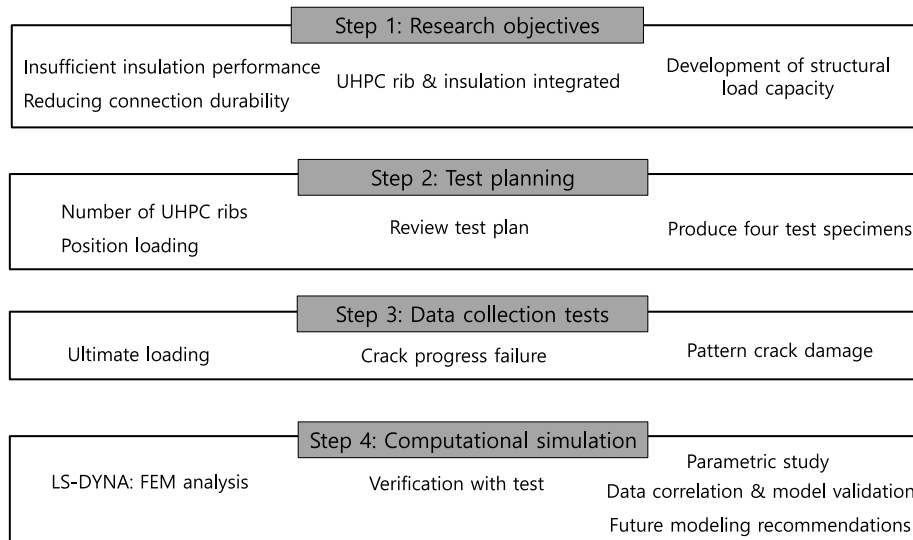


Fig. 3. Steps for preparing research methodology.

Table 2
Detailed information on test specimens.

No	Specimen	Extrusion SK (mm)	Applied loading	Thickness slab (mm)	Number SK	Number rib	Rib width (mm)
1	LBN-RIB4-150-S	20	Shear	150	1	4	55
2	LBN-RIB4-150-F	20	Bending	150	1	4	55
3	LBN-RIB5-210-S	20	Shear	210	2	5	55
4	LBN-RIB5-210-F	20	Bending	210	2	5	55

SK is shear key.

consistent throughout the experiment. This ensured that these variables did not influence the results of the study.

The process for assembling the UHPC rib formwork is shown in Fig. 4. To produce the UHPC rib, the cement was mixed in the laboratory and allowed to cure for one day after pouring. The components were then processed, assembled, and connected to the slab and PC wall after being treated with steam at 40 °C for 14 h. To obtain the desired strength, prefabricated UHPC ribs were cured for 28 days. This figure displays the process of making the specimen by mixing the UHPC and preparing the formwork, followed by placing the UHPC in the formwork. The ribs were then fitted and joined after preparing and assembling the insulation.

2.3. Experiment test set-up

The general geometry of the test specimens is depicted in Fig. 5, and details of the geometrical and configuration of the UHPC shear key connection PC wall are given in Fig. 6. The size of the slabs were 1920 × 1000 × 150 mm³ (length × width × thickness), and 1920 × 1000 × 210 mm³ (length × width × height), respectively. Horizontal and vertical PC walls were reinforced with D13 mm rebars spaced at 200 mm intervals. In addition, all slabs in the specimens were reinforced with D13 main directional bars spaced at 200 mm intervals, along with D13 secondary directional bars spaced at 300 mm intervals [26].

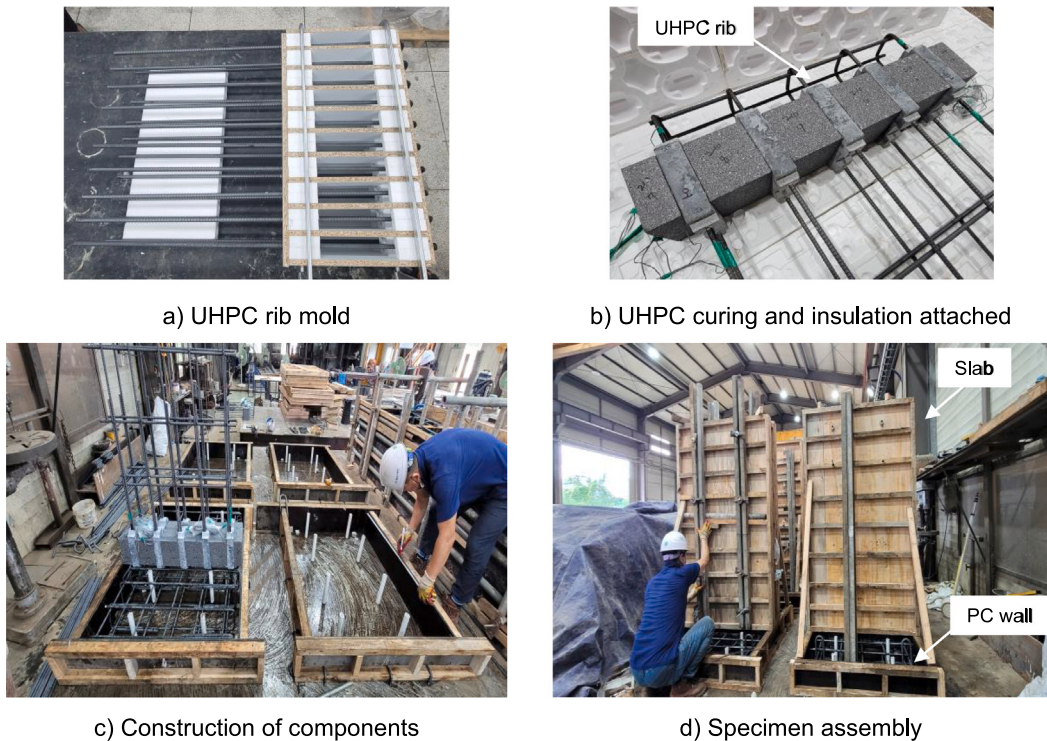


Fig. 4. Construction process of specimens.

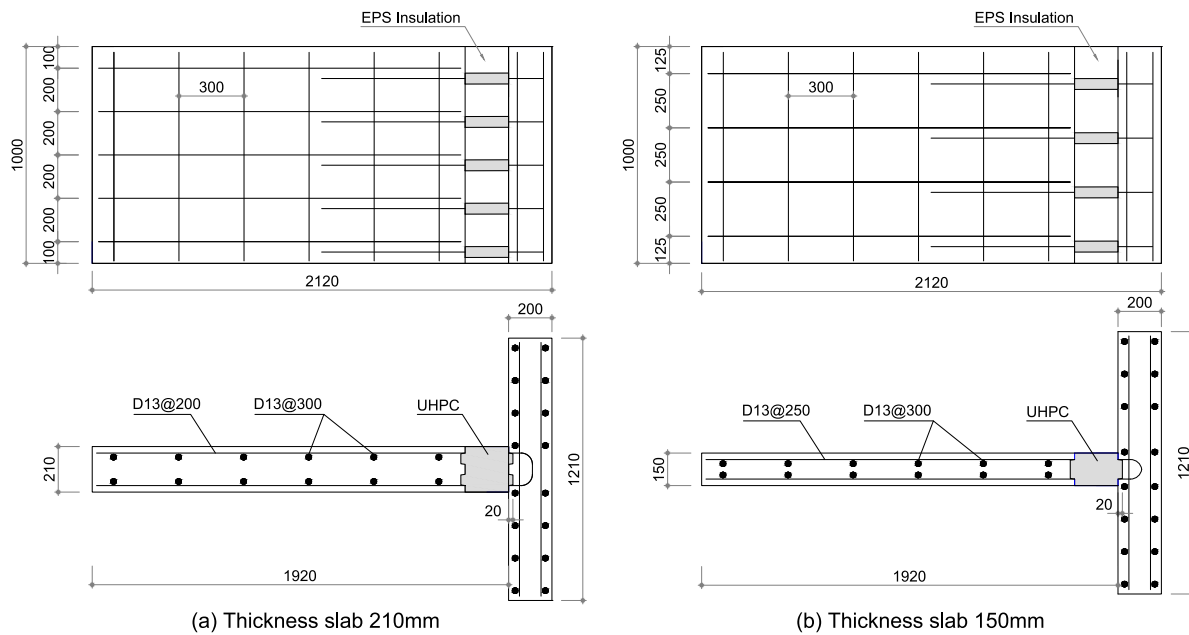


Fig. 5. Dimensions of specimens.

2.4. Instrumentation

A load distribution beam, subjected to a hydraulic loading cylinder in the middle was put on the slabs. The specimen was subjected to a constant displacement rate of 5 mm/min. A linearly variable differential transducer (LVDT) was also installed to measure the displacement of the slab and ribs vertically with loading. Four LVDTs were installed on the lower face of the slab. The mounting positions of the LVDTs are shown in Fig. 7. They were placed in the same positions in each case to allow comparison of the different performances and behaviors. The

displacement measurements for the tests are recorded at positions A and B, with point A assigned to the bending test and point B to the shear test. Regarding the shear test, the experimental results are influenced by the bending moment. Based on the condition of the test facilities, as well as the distance between the experimental loading application point and the PC wall is minimized, it is assumed that the test is a pure shear test under these conditions. In this study, adopting this approach is deemed appropriate, it enables an efficient arrangement for conducting shear tests.

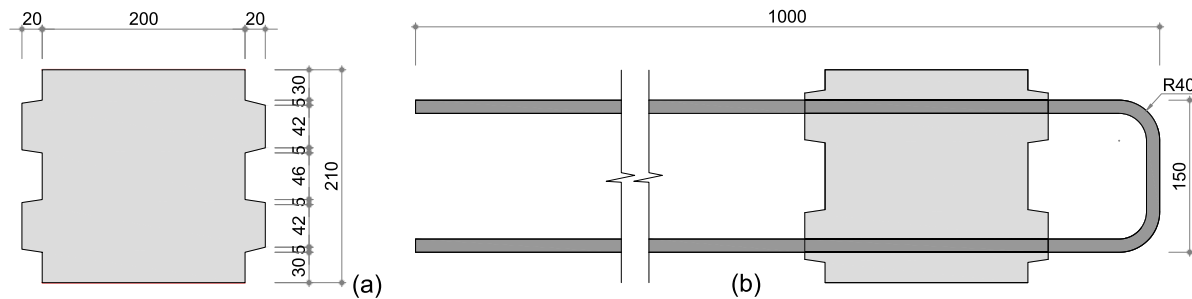


Fig. 6. Dimensions of connection details: (a) number shear key (b) UHPC rib.

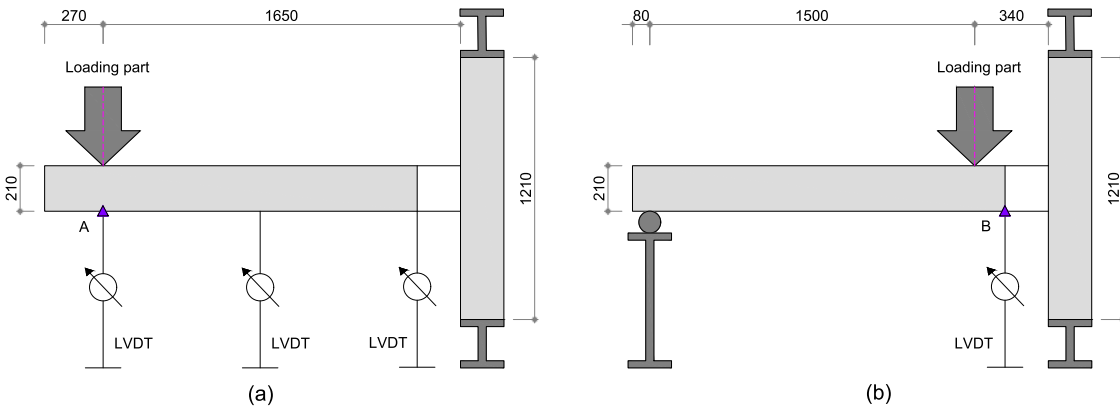


Fig. 7. Test setup slab thickness of 210 mm: (a) bending; (b) shear.

3. Experimental results and discussions

3.1. Tests observations and failure modes

Fig. 8 shows the failure mode of specimens during testing. During the shear strength test of LBN-RIB4-150-S, cracks appeared between the UHPC rib and inner wall, forming a V shape at the lower center of the plate due to increased shear force. The first plastic joint occurred at the rib and wall joints, and as load increased, shifting occurred at the beam end. Damage occurred more frequently between the rib and slab than between the rib and wall connections, which can be attributed to the potential influence of a small bending moment on this observed behavior. Another contributing factor was the difference in the connection between the UHPC rib and slab compared to that between the UHPC rib and the PC wall. However, the connections embedded in the UHPC rib and wall showed sufficient resistance to shear forces. For LBN-RIB5-210-S, the initial shear resistance was focused on the joints between the rib and wall, where a plastic joint forms. Afterward, the plasticization occurred again, with deformation in the middle. Cracks and damage occurred more frequently between the ribs and slabs than between the connections of the ribs and walls. The steel connections that are embedded in the UHPC rib and attached to the wall exhibited adequate resistance to shear forces.

The test conducted on LBN-RIB4-150-F recorded a maximum load of 28.34 kN with a corresponding displacement of 113.27 mm, and the maximum displacement reached was 205.23 mm. The cantilever experienced a negative moment, leading to cracks that initially formed near the wall and spread towards the center. The cracks in the upper part of the slab were caused by the destruction of the reinforced anchor of the UHPC rib. More cracks and damage were observed between the panels than in the connection between the ribs and the wall, likely due to concentrated stresses and strains between the floor slab and the wall. For LBN-RIB5-210-F, cracks initially appeared near the PC wall and spread towards the center of the plate with an increase in load. The reinforced anchor of the UHPC rib was destroyed, resulting in the

breaking of the upper part of the plate and reducing the bond between the wall and the PC plate. However, the stirrup embedded in the UHPC rib and attached to the wall was strong enough to withstand flexure.

3.2. The behavior of shear key

The influence of the number of shear keys was investigated by testing two specimens. Fig. 9 shows the crack patterns of these specimens. Results showed that the shear strength increased by 56.85%, from 311.13 kN to 488.01 kN, when the number of shear keys increased from one to two and the ribs from four to five. However, in general, the dimensional parameters of the shear key had minimal impact on the ultimate shear-bearing capacity of the structures. The crack patterns observed for the LBN-RIB4-150-S and LBN-RIB5-210-S cases differed for one shear key versus two shear keys. For the LBN-RIB4-150-S, the initial crack appeared at the upper corner of the key and extended vertically and horizontally. This resulted in a separation between the upper portion of the key and the base of the joint, leading to the detachment of the concrete connecting the top of the key with the slab. In the case of the 2 shear keys LBN-RIB5-210-S, similar crack patterns to LBN-RIB4-150-S were observed, but in addition, several shorter diagonal cracks emerged near the keys. During the experiments, failure mechanisms were found on the slab area. The load capacity of the connection between the UHPC rib and PC wall were found to be significantly influenced by the number of shear keys and loading position.

3.3. Load-displacement curves

Fig. 10 shows the test results for the shear and bending specimens as a graph of the relationship between force and displacement. Table 3 provides data on load capacity, displacement, value of the 75% ultimate load, and initial stiffness of the four specimens. During the tests, the load-displacement curves were continuously recorded. For the shear specimen, the test load of the LBN-RIB5-210-S was approximately 180



Fig. 8. Failure mode of experimental specimens.

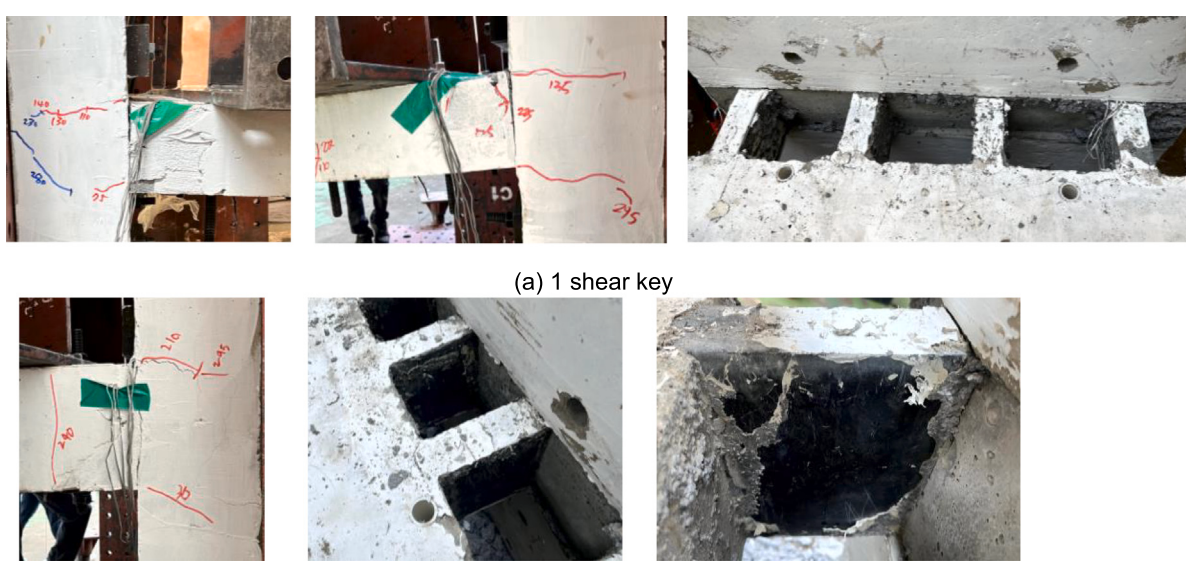


Fig. 9. Damage crack pattern.

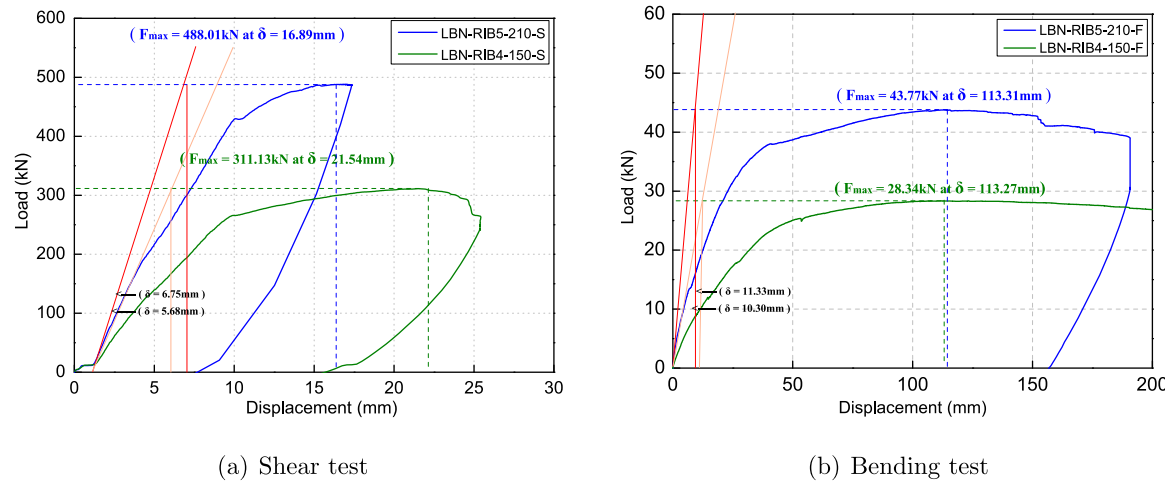


Fig. 10. Load-displacement curves of the experiment.

Table 3
Summary of the experimental test results.

Specimen	Load (kN)	Disp. (mm)	75% load (kN)	75% disp. (mm)	Initial stiffness (kN/mm)
LBN-RIB4-150-S	311.13	21.54	233.35	8.34	54.77
LBN-RIB5-210-S	488.01	16.89	366.00	8.51	72.29
LBN-RIB4-150-F	28.34	113.27	21.25	34.81	2.75
LBN-RIB5-210-F	43.77	113.31	32.82	27.30	3.86

kN higher than that of LBN-RIB4-150-S, corresponding to a 56.85% increase. Displacement was also reduced by 4.65 mm, representing a 21.58% decrease. In terms of initial stiffness, LBN-RIB5-210-S was greater than LBN-RIB4-150-S. For the LBN-RIB4-150-F and LBN-RIB5-210-F specimens, the load capacities were 28.34 kN and 43.77 kN, respectively. The specimen with two shear keys and five ribs had a higher load capacity, up to 1.54 times greater than the specimen with a single shear key and four ribs. As can be seen, the displacement for both specimens was similar in two of these cases, with values of 113.31 mm and 113.27 mm, respectively. The initial stiffness was 2.75 kN/mm and 3.86 kN/mm, respectively.

3.4. Discussion in terms of the shear capacity formula

The problem of shear failure of concrete shear key joints has been considered in previous studies. Methods proposed by AASHTO, JSCE, and the formula proposed by Rombach and Specker are used to calculate shear capacities of structure [27–32]. Kaneko et al. developed a mechanical model for the analysis of concrete shear key joints [33,34]. In this work, shear capacity calculations are conducted using methodologies by AASHTO, JSCE, and Rombach and Specker. The AASHTO proposes a formula

$$V_u = A_k \sqrt{f_{ck}} (0.2048\sigma_n + 0.9961) + 0.6A_{sm}\sigma_n \quad (1)$$

where V_u denotes shear strength; A_k denotes the area of all keys; f_{ck} denotes the compressive strength of concrete; σ_n denotes average compressive stress at the joint plane.

The formula of Rombach and Specker is as follows:

$$V_j = 0.14f'_c A_k + 0.65 (A_k + A_{sm}) \sigma_n \quad (2)$$

where f'_c denotes the compressive strength of concrete and A_{sm} denotes the contact area without shear key.

The JSCE formulation is given by

$$V_{cw} = \mu f'_{cd} \sigma_{nd}^{1-b} A_{cc} + 0.1 A_k f'_{cd} \quad (3)$$

Table 4
Summary of shear capacity in the design formulation (Unit: kN).

No	Specimen	AASHTO	Rombach & Specker	JSCE
1	LBN-RIB4-150-S	188.7	305.7	528.0
2	LBN-RIB5-210-S	263.8	406.8	679.6

where μ denotes average contact friction coefficient ($\mu=0.45$); f'_{cd} denotes compressive strength (MPa); σ_{nd} denotes average compressive stress; A_{cc} denotes area of shear plane in compression zone; b coefficient represents the configuration of planes and ranges between 0 and 1.

Table 4 compares the shear capacity of different structures using the equations proposed by AASHTO, Rombach and Specker and JSCE. It shows that the JSCE formula overestimates the shear capacity of the UHPC rib, while the AASHTO formula undervalues the shear capacity of the structures. The Rombach and Specker formulation suitable approximates the results of the tests performed. The discrepancies in the results can be attributed to factors such as the shape of the shear keys and the concrete strength of the PC wall. The test specimens employed two different types of concrete with significantly different strengths, 160 MPa and 27 MPa, which could lead to different results. In addition, variations in specimen sizes and test conditions might cause discrepancies in the obtained standards. Different criteria may be used in standards to examine the geometry and details of structural components.

4. Numerical analysis

4.1. FE model procedure

Initially, the system's behavior is modeled under various conditions using the FE model, which involves discretization. Subsequently, results obtained from the FE model are compared with previously collected experimental data, with model parameters being adjusted for validation. Furthermore, key design parameters such as concrete strength and yield strength are systematically varied while keeping others constant to assess their specific impacts. Ultimately, data correlation is employed to validate the simulation model, ensure its accuracy, and identify crucial parameters for replicating real behavior.

4.2. General

In a FE analysis, parameters such as shape and the number of shear keys, size, concrete strength, and yield strength of steel are studied to consider their influence on load capacity. To investigate

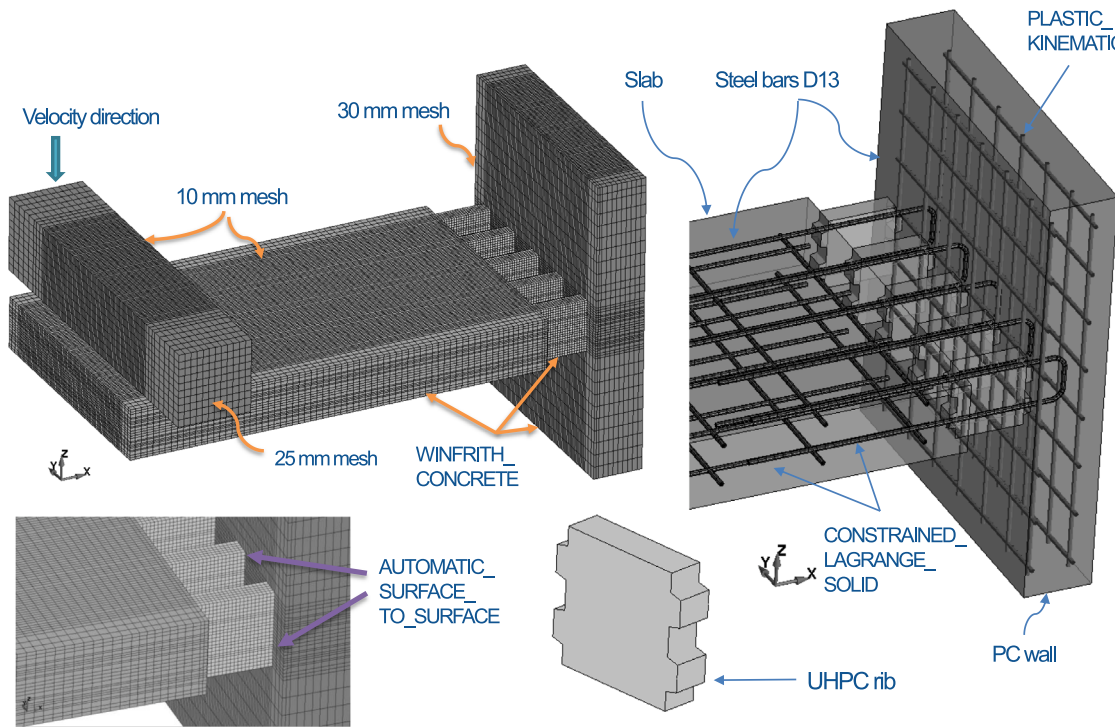


Fig. 11. Numerical model of bending tests.

the shear and bending behavior of the structures in more detail, four models were created using LS-DYNA program to determine the ultimate load [35]. The Winfrith model was selected. The accuracy of the model was confirmed by comparing its results with those obtained from the experimental tests.

The influence of concrete strength and the yield strength of the rebar on the shear and bending behavior of structures was investigated using a parametric study [36]. The FE model used in the study consisted of four components: a precast concrete PC wall, an ultra-high performance concrete rib, a slab, a rigid loading part, and rebars. The UHPC, PC wall, and slab were modeled using the Winfrith model. Rebars can be modeled using the MAT03 model. The MAT020 model was used to simulate the loading part as a rigid material [37,38]. In this study, assumptions of perfect bonding between the concrete and steel reinforcement were defined by the Lagrange-In-Solid constraint [39]. In addition, contact between conventional concrete, UHPC, and loading part were defined as the Surface-To-Surface function while the scale factor on slave, master penalty stiffness (SFS, SFM) equaled 1.0. The boundary condition was used to apply nodal restrictions.

4.3. FE model development

4.3.1. Element type and mesh size

The models used for the bending and shear specimens are presented in Figs. 11 and 12. For modeling the UHPC rib, slab, and PC wall, an eight-node solid element was employed, whereas a beam element was utilized to model the rebars. The mesh size used in the models depended on the size and shape of the specimens being analyzed. In this particular study, mesh sizes of 10 mm (slab, UHPC), 25 mm (rebar), and 30 mm (PC wall) were used [40,41].

4.3.2. Contact and boundary conditions

The vertical loads were applied to the slab using a solid rigid plate. Plate deformation was prevented by assigning a rigid material properly

to their loading. In LS-DYNA, the prescribed motion for the rigid portion of the plate was defined and implemented using the Prescribed-Motion-Rigid option. The set of nodes in the PC wall were subjected to fixed, supported boundary conditions. Fixed supported boundary conditions were applied to the set of nodes in the PC wall. Meanwhile, the movements were also restrained following the translation in the Z axis and rotation around the X and Y directions at the end of the slab for bending simulation, as shown in Figs. 11 and 12. The reinforcements were embedded in the concrete, which was modeled using the Lagrange-In-Solid option. This simulates a perfect bond between the reinforcement and concrete and ignores bond-slip behavior. The contact surface was modeled using the Surface-To-Surface function. In all cases, the part of the model was defined as either slave or master. These contacts were checked for penetration on either side of the element. The process of checking for contact involves reversing the roles of the master and slave in a two-way contact, as illustrated in Fig. 13. In cases where no slave nodes are detected upon projection onto the master surface, as illustrated in the figure below, penetrations may occur.

4.3.3. The Winfrith concrete model

The Winfrith model was employed to simulate the concrete behavior. This model provides unconstrained compression and tensile strengths to generate output data that includes the size and location of cracks in the concrete [43]. By inputting the concrete compressive strength into the model, all of the necessary parameters are automatically generated. The ability to provide information about crack propagation in concrete is one of the most crucial features of this capability. It is important to note that the input parameter for tensile cracking must be specified. When strain rate effects are disabled, this parameter determines the width of the crack when the normal tensile stress is zero. The crack width formula used in this model is dependent on the crack opening displacement. As the fracture opening displacement increases, the length of the crack expands and propagates,

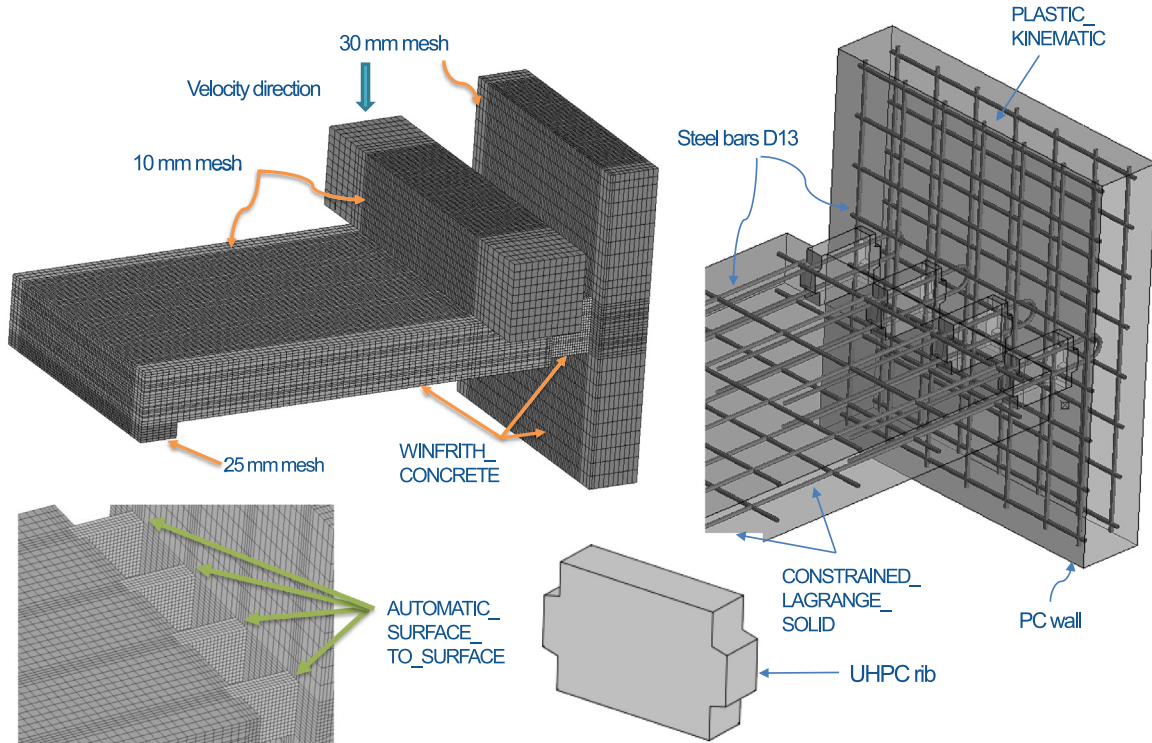


Fig. 12. Numerical model of shear tests.

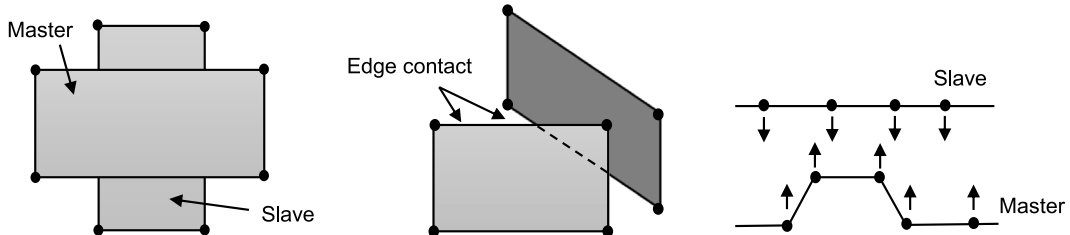


Fig. 13. Two-way contact define [42].

Table 5
Input parameters in the Winfrith concrete material model.

Parameter	Poisson's ratio	Density (g/mm ³)	Compressive strength	Tensile strength	Crack width FE	Aggregate size
Value	0.17	0.0023	20	2.504		
			25	2.800		
			27	2.909		
			35	3.313	0.2	
			40	3.541		20

resulting in the creation of a new crack surface. The specific fracture energy is shown in Fig. 14. The crack width w is represented by a constant c .

$$c = w \frac{f_t}{G_f} \quad (4)$$

where G_f denotes specific fracture energy, f_t denotes tensile strength.

Several input parameters are displayed in Table 5. Note that the units of compressive and tensile strength are MPa. Crack width and aggregate size are mm.

4.3.4. Steel model

The reinforcing rebars were modeled using the MAT03 model, which can simulate simultaneously isotropic and kinematic hardening plasticity, as shown in Fig. 15, where Etan represents the hardening stiffness of the bilinear stress-strain curve and β denotes the hardening ranging from 0 to 1. Table 6 presents some of the input parameters. For reinforcing bars, a mesh size of 25 mm was employed. The Lagrangian solid method was used to define a perfect bond between the reinforcement steel and concrete at the nodes where they intersect, using constraints. In these simulations, the tops of the slabs were assumed to

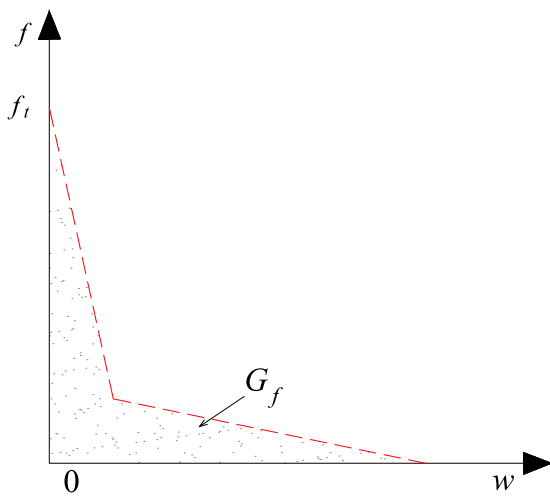


Fig. 14. Crack strain softening response in Winfrith model [44].

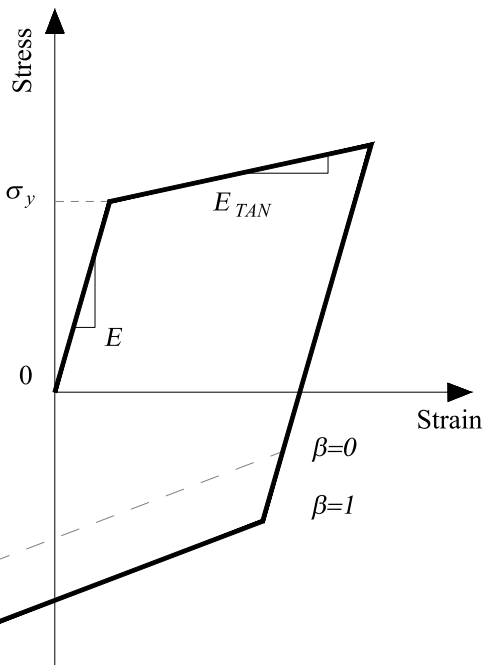


Fig. 15. Stress-strain curve of rebar in the numerical simulation.

Table 6
Parameter properties of the MAT03 model.

Material	Poisson's ratio	Density (kg/m ³)	Young's modulus (GPa)	Yield strength (MPa)
D13	0.260	7830	180	502

be rigid and used to apply the loading. The loading part was modeled using MAT020 model.

5. Validation of the numerical model

5.1. Ultimate load-displacement curves

The numerical results agreed well with the test results and indicated similar values for the initial stiffness, elastic range, and ultimate load. Fig. 16 illustrates the load-displacement curves and the corresponding

values that were obtained from the numerical model. These results were compared to the experimental data from the four specimens to validate the accuracy of the developed FEM. The predicted load-displacement curves had a shape that was comparable to the measured response. The peak load obtained from the numerical model for all specimens was similar to the experiment test, with little variation between the two. Peak loads in the numerical model of about 313.20 kN, 28.12 kN, 510.69 kN, and 46.80 kN were obtained at around 29.89 mm, 74.90 mm, 20.91 mm, and 92.60 mm, respectively. The discrepancies between the simulated peak loads and test results were 0.66%, 0.77%, 4.64%, and 6.92%, respectively.

The LBN-RIB4-150-S and LBN-RIB5-210-S specimens showed numerical displacement values of 29.89 mm and 20.91 mm, respectively. The numerical load values for these specimens were 313.20 kN and 510.69 kN, respectively. The percentage discrepancies between the experiment and FE model displacement values were 27.93% and 19.22%, respectively. While load values were 0.66% and 4.64%, respectively. These values clearly demonstrate that there are differences in the behavior of the two specimens under load. Specifically, the LBN-RIB5-210-S specimen exhibited less displacement and greater load capacity compared to the LBN-RIB4-150-S specimen.

The LBN-RIB4-150-F specimen displayed greater percentage errors in displacement compared to the LBN-RIB5-210-F specimen, while demonstrating smaller percentage errors in load. The numerical model of the LBN-RIB4-150-F specimen resulted in a displacement value of 74.9 mm with a percentage error of 33.23%, and a load value of 28.12 kN with a percentage error of 0.77%. On the other hand, the numerical model of the LBN-RIB5-210-F specimen produced a displacement value of 92.60 mm, which resulted in a percentage error of 18.27%, and a load value of 46.80 kN, with a percentage error of 6.92%. Table 7 presents both the experimental and numerical data for the displacement and load of the four specimens, along with their respective percentage errors. The percentage errors for displacement ranged from 18.27% to 33.23%, while the percentage errors for load were between 0.66% and 6.92%.

For the most part, the shapes of the load-displacement curves generated by the numerical model were similar to the experimental results. However, for the LBN-RIB4-150-S specimen, there was a discrepancy in the elastic range compared to the experimental data. During the simulation, neglected factors such as the bond-slip behavior between the concrete and rebar and the hourglass effect, as well as other factors, can lead to an excessively high initial stiffness in the numerical model. The hourglass effect refers to an undesirable numerical instability phenomenon that can occur during FE simulations. It appears in elements as a local distortion or hourglass-shaped deformation pattern. This effect can lead to inaccurate results and compromise the accuracy of the simulation, necessitating the use of appropriate numerical stabilization techniques to reduce its impact. The overall results obtained from the numerical simulation were deemed acceptable. The results showed that the models accurately predicted the relationship between load and displacement for concrete. Thus, the numerical model method employed is sufficiently accurate to predict the ultimate load capacity and the behavior of concrete in structures.

5.2. Failure behavior

For the LBN-RIB5-210-S and LBN-RIB4-150-S models, the typical phenomena from the model are compared with the experiment results, as depicted in Figs. 17a and b. The crack pattern and concrete spalling at the top and bottom of the slabs in the two models are displayed in the figures. It can be seen that the slabs in the model suffered cracks and concrete spalling at the same position as the experiment. The main cracks were observed on the edge of the model. Some cracks of varying widths developed, and the dimensions of these cracks increased with increasing loading rates. The test showed that some minor cracks appeared on the top surface of the slab. This indicates that the reason for

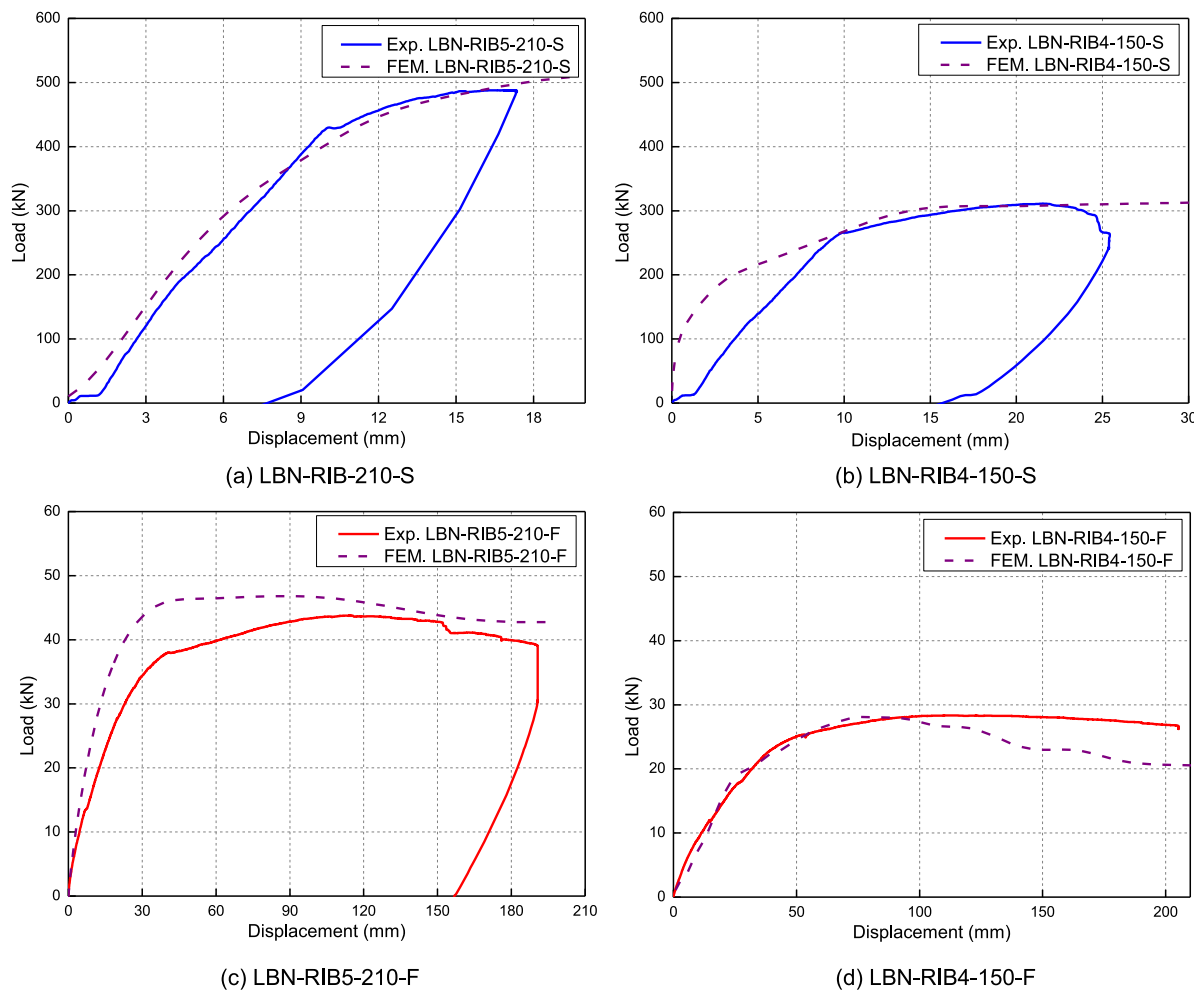


Fig. 16. Comparison between experimental and numerical results.

Table 7
Summary of the numerical and experimental results.

Specimen	Displacement (mm)			Load (kN)		
	Experiment	Numerical	Error (%)	Experiment	Numerical	Error (%)
LBN-RIB4-150-S	21.54	29.89	27.93	311.3	313.2	0.66
LBN-RIB4-150-F	112.18	74.9	33.23	28.34	28.12	0.77
LBN-RIB5-210-S	16.89	20.91	19.22	488.01	510.69	4.64
LBN-RIB5-210-F	113.31	92.6	18.27	43.77	46.8	6.92

the failure of the specimen was the stress concentration phenomenon at the bottom of the UHPC rib, where failure first occurred. In addition, the FE model crack length and width were in good agreement with the test results.

The fracture pattern of the LBN-RIB5-210-F and LBN-RIB4-150-F models can be seen in Figs. 17c and d, respectively. The crack pattern is visible on the top surface of the slab, which is a result of the simulation used to create these models. During the simulation, it was observed that most of the damage occurred around the intersection of the slab and UHPC rib, as well as in the middle of the slab. One advantage of using the FE model is that it allows the crack pattern to be viewed inside the specimen. This is not possible through direct observation by eye during testing. The shape of the UHPC rib remained nearly unchanged during testing, while the slab showed obvious flexural cracks in several positions on the left, right, bottom, and top sides. Major cracks and notable fractures were observed at the top and bottom of both specimens, consistent with the test results. The Winfrith model was able to predict the behavior of the concrete with acceptable accuracy.

In both situations, there was minor local stress that emerged on the lower part of the shear keys. The damaged concrete area resembles the cracks observed during testing. In contrast, the section where the shear keys connect to the slab experienced concrete damage that expanded upward to the top of the shear keys. Fig. 18 shows that the stress on the top of the shear keys was lower than that on the bottom, indicating that shear failure progressed from the lower part to the upper part of the shear keys connected to the PC wall. Conversely, for shear keys connected to the slab, the opposite result was observed.

Although the tests and models showed little difference, some factors may explain the variations observed between the numerical and experimental results. One such factor is the softening process of the material in the constitutive model, which may differ slightly from the actual observed behavior. As a result, future research will focus on modifying the constitutive model for UHPC, including the hourglass and bond-slip behavior between concrete and rebar. Table 8 lists several critical input parameters. These recommendations include modifications to the constitutive model and the parameters for each component in the model [45]. This work provides parameters and results for evaluating

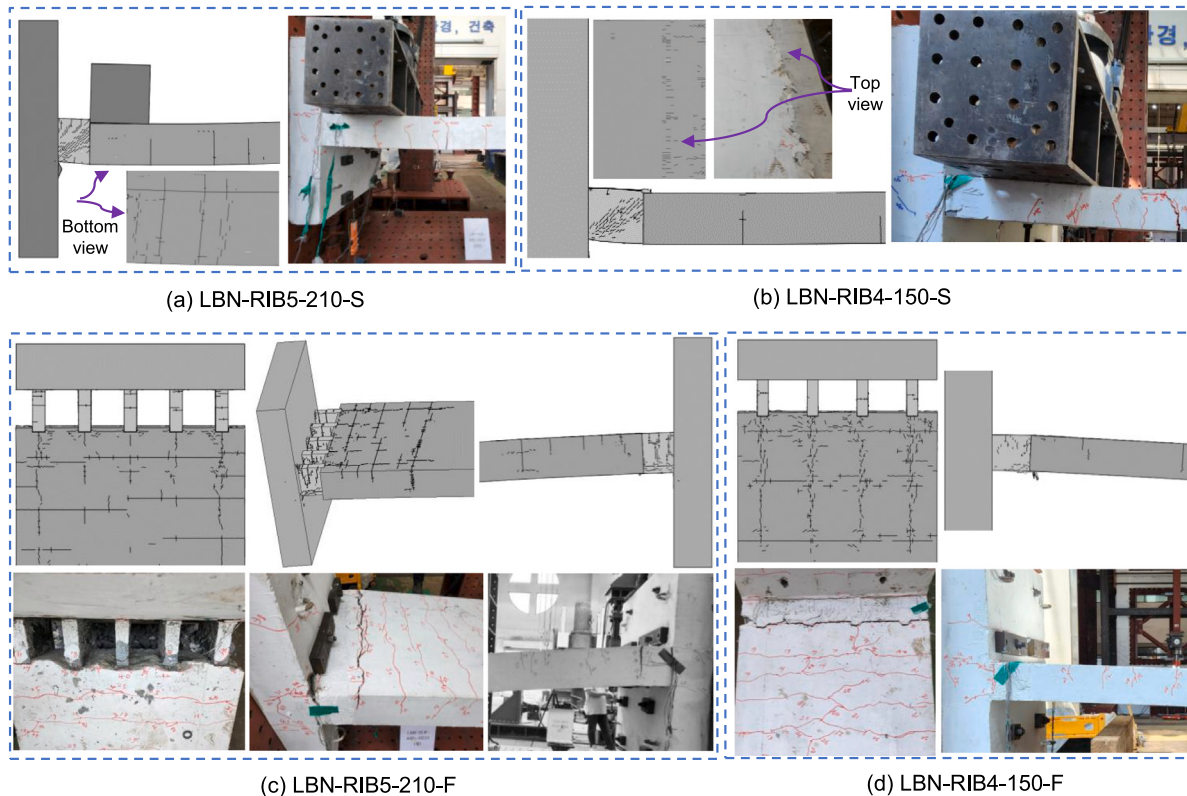


Fig. 17. Comparison of the crack failure of specimens in the test and numerical model.

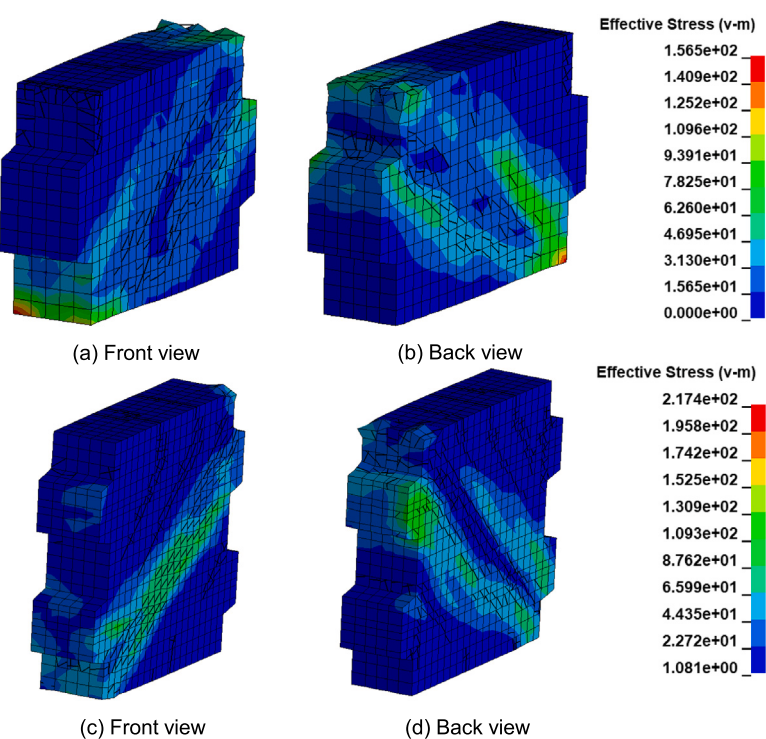


Fig. 18. Effective stress for shear keys: (a),(b) LBN-RIB4-150-S ; (c), (d) LBN-RIB5-210-S.

Table 8
Modeling recommendations.

Component	Constitutive model	Parameter	Value
UHPC, concrete Reinforcing steel	Winfrith MAT03	Table 4, RATE 0 Hardening parameter	Default 0.2
Loading part Contact	MAT020 Surface-To-Surface	SFS, SFM	1
Bar-concrete interface		Perfect bond, Lagrange-In-Solid	

SFS and SFM are scale factor slave and master penalty stiffness, respectively.

the precision of modeling methods for both reinforced concrete and rebars. These results and recommendations, which include the constitutive model, bar-concrete interface, conventional concrete value, and reinforcing steel, can be beneficial to other researchers using the LS-DYNA program.

6. Parametric analysis and discussion

The validated FE model was utilized for a parametric study on the structural performance of LBN-RIB5-210-S and LBN-RIB4-150-F. The study focused on investigating the effect of concrete strength on the ultimate load capacity of the models. The parameters considered in the investigation were unconfined compressive strength (f'_c) of UHPC rib $f'_{c(UHPC)} = 60\sim180$ MPa, slab $f'_{c(PC)} = 25\sim40$ MPa, and steel rebar $f_y = 387\sim659$ MPa. A total of 29 scenarios were conducted, with the geometry of the specimens remaining constant. Furthermore, seven scenarios were conducted to investigate the impact of geometric parameters, specifically the thickness of the slab and UHPC rib.

6.1. Effect of concrete compressive strength on the slab

The numerical simulations aimed to investigate the effect of concrete compressive strength on the behavior of the slab. The simulations were carried out while keeping the concrete strength of the UHPC rib, the yield strength of rebars, and other parameters constant. For LBN-RIB4-150-F, the results demonstrated that raising the concrete compressive strength from 20 MPa to 40 MPa increased the peak load of the slab. The highest peak load of 28.4 kN was recorded for the 40 MPa strength, while the lowest performance was 25.7 kN, corresponding to 20 MPa, which is a 10.5% enhancement, as depicted in Figs. 19a and 20a. Similarly, the peak loads of LBN-RIB5-210-S increased from 496 kN to 532 kN, depending on the concrete strength used. Overall, increasing the concrete strength led to an increase in peak loads for both models. The displacement values for the different concrete strengths ranged from 20.4 mm to 21.6 mm. For LBN-RIB5-210-S, the load-displacement curves showed similar shapes, while for LBN-RIB4-150-F, the curve changed after reaching the ultimate load, indicating a different tendency. Based on the results, it can be concluded that using normal concrete at 27 MPa is suitable in terms of design and economics.

6.2. Effect of the compressive strength of the UHPC rib

Concrete with a compressive strength of 60 MPa and 90 MPa is not considered as UHPC. However, with the aim of understanding the behavior and load capacity of the overall structure while altering the concrete strength of the rib. As a result, this section takes into account two scenarios. As shown in Figs. 19b and 20b, an increase in the concrete strength of LBN-RIB4-150-F from 60 MPa to 180 MPa resulted in an increase in peak load from 23.8 kN to 27.9 kN, indicating an increment of up to 17.2%. Similarly, the ultimate shear capacity of LBN-RIB5-210-S increased by about 26.7%, from 412 kN to 522

kN, according to variation in the strength of the UHPC. The load-displacement curve indicated some nonlinear changes, with a minimal change in shape observed for LBN-RIB5-210-S. Overall, these results highlight the potential of using concrete with high strength to enhance load capacity while reducing material usage.

6.3. Effect of steel strength

The correlation between load and displacement in the model is illustrated in Figs. 19c and 20c. The results indicate that as the steel strength rose from 387 MPa to 659 MPa, the ultimate load of the specimen slightly increased by 4.19% and 4.95% for LBN-RIB4-150-F and LBN-RIB5-210-S, respectively. However, it is observed that the improvement in the ultimate load was not significant with an increase in f_y . The highest ultimate load values were 29.3 kN and 536 kN, while the lowest values were 27.3 kN and 507 kN for LBN-RIB4-150-F and LBN-RIB5-210-S, respectively. Therefore, the effect of steel strength on the results in these cases was minor. Further research is recommended to investigate the effect of varying steel strength values on the structures.

6.4. Effect of strain rate

Numerous parameters can affect a model's response, and the strain rate has a direct effect on the behavior of concrete. The rate effect describes the dependency of material on loading or strain rates. Within LS-DYNA, the impact of strain rate on concrete strength is captured through an inherent parameter derived from multiple concrete models. The Winfrith model, which focuses on various rate effects, was studied in terms of RATE = 0, RATE = 1, and RATE = 2; strain rate effects are included (RATE = 0), strain rate effects are turned off (RATE = 1), and RATE = 2 is similar to RATE = 1 but includes an improved crack algorithm. The RATE parameter in these models determines the rate sensitivity of the material. RATE values of 0, 1, and 2 reflect varying levels of rate sensitivity in the behavior of the material. The strain rate of the model was analyzed, and the results indicated that the model performed best with RATE = 0, as shown in Figs. 19d and 20d. These findings were validated by four experiments in the study. Overall, the strain rate effect is an important consideration when modeling materials, as it can have a significant impact on the accuracy and reliability of simulation results.

6.5. The effect of the slab and UHPC rib thickness

In this section, the effect of geometric parameters on the overall structural performance is studied. It can be noted that during analysis, concrete strength, yield strength of reinforcement, position, and loading direction are all kept constant. Four cases of the LBN-RIB5-210-S model were taken into consideration, encompassing varying dimensions of the slab and UHPC thickness, namely 180 mm, 230 mm, 270 mm, and 300 mm. Also, three cases of the LBN-RIB4-150-F model with thicknesses of 170 mm, 190 mm, and 210 mm were conducted.

Fig. 21a clearly shows that the response provided by the 300 mm case is the highest among the four cases, while the case with a thickness of 180 mm is the lowest. The ultimate loads are 418.3 kN, 513.8 kN, 593.4 kN, and 679.5 kN, respectively. At the same time, the displacements are 19.4 mm, 16.7 mm, 23.3 mm, and 18.1 mm. The maximum load of the 180 mm case is 14.3% lower compared to the specimen test with a thickness of 210 mm, whereas the remaining cases are 5.12%, 21.5%, and 39.1% higher. There is a significant difference in the ultimate load. As shown in Fig. 21b, the maximum loads of the H150-F are 30.8 kN, 32.9 kN, and 34.7 kN, respectively, exceeding the load of the specimen test at 28.34 kN. Simultaneously, the corresponding displacements are 69.1 mm, 58.3 mm, and 43.6 mm, respectively. The ultimate load of the model is significantly enhanced by changing the slab and UHPC rib geometry, with ultimate loads 8.7%, 16.1%, and

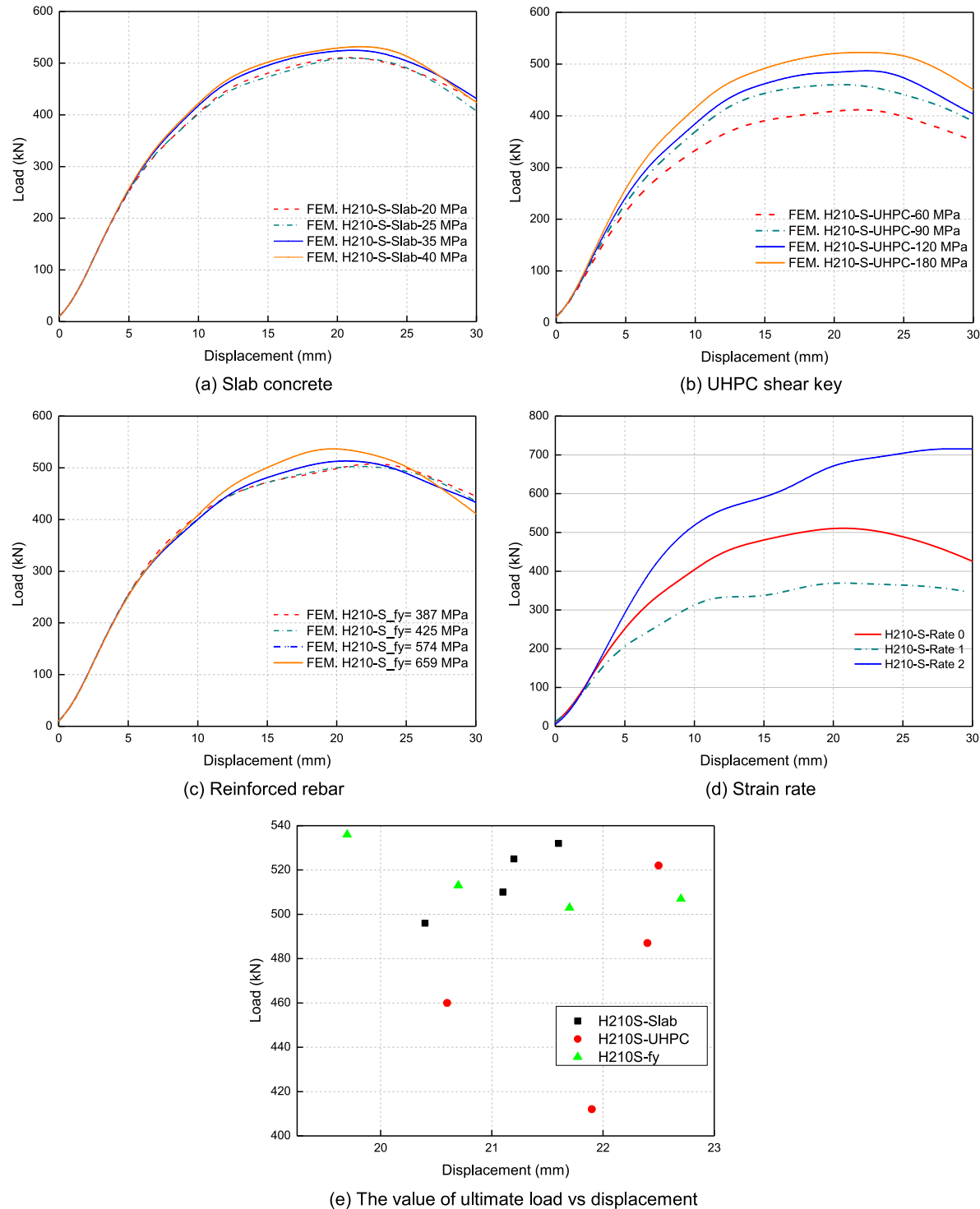


Fig. 19. Parametric results for the LBN-RIB5-210-S case.

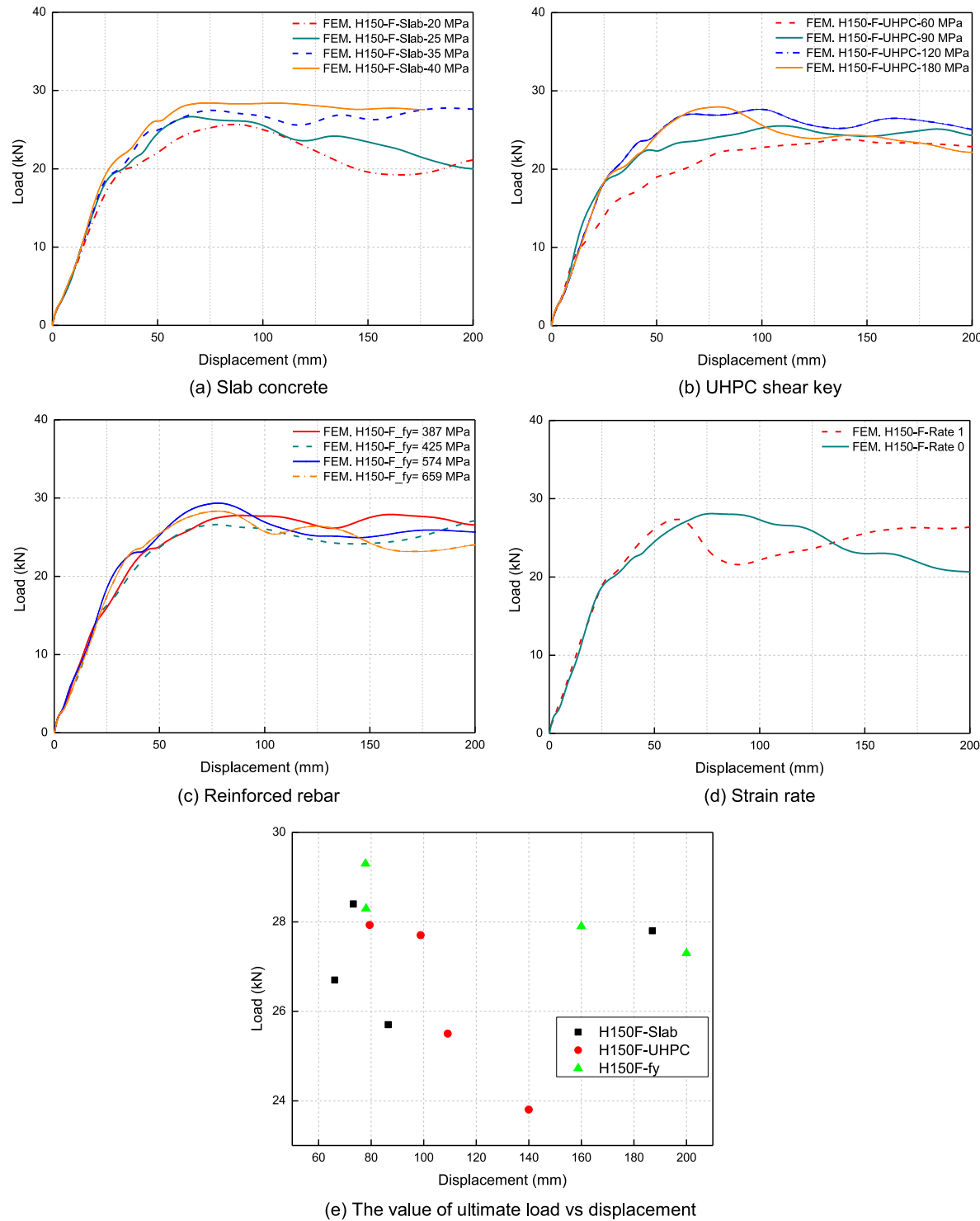


Fig. 20. Parametric results for the LBN-RIB4-150-F case.

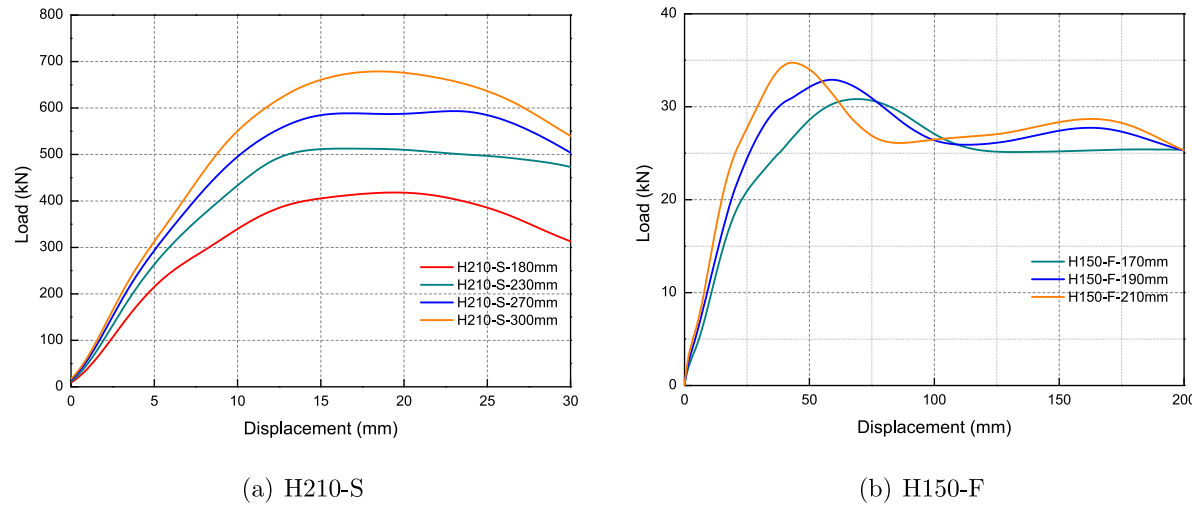


Fig. 21. The results of geometric analysis.

22.5% higher than the specimen test. After reaching the peak load, a rapid decrease in load is observed with further increased displacement.

The load-displacement curves of all cases are plotted in Fig. 21. As can be seen, the observed differences are substantial in terms of the ultimate load. Generally, when the thickness of the slab and UHPC rib increases the ultimate load of the specimen tends to be raised in all cases. It can be concluded that the ultimate load is significantly influenced by the change in geometry. The findings of this study can be used for optimizing the shape of the slab and UHPC rib to design in apartment buildings.

6.6. Predicted crack and failure pattern

As shown in Appendices A and B, LS-DYNA was able to detect the cracks that developed in the concrete from the 36 scenarios. The numerical analyses revealed that cracking occurred at the intersection position between the UHPC rib and the slab in all cases. The types of cracks observed in the LBN-RIB4-150-F models were similar despite variations in the concrete strength. As the peak loads increased, these cracks propagated towards the end of the slab. Additionally, it was observed that the majority of the cracking occurred around the 1/2 length point of the slab, with cracks along the slab at the position of the UHPC ribs. For the LBN-RIB5-210-S model, which had two shear keys, the cracks occurred in the bottom positions of the slab. There was a slight difference in the analytical results, which showed that the cracks extended towards the two side surfaces of the wall. Two major cracks were found to develop in the horizontal slab at the bottom. Moreover, the majority of the crack types were minor cracks and discontinuous. When the thickness of the slab and UHPC rib were adjusted, there was a significant reduction in the number of cracks on the UHPC, with minor cracks visible in the LBN-RIB4-H150-F model. Simultaneously, a reduction in cracks along the UHPC rib was observed. The reduced occurrence of cracks can be attributed to the increased thickness of both the slab and the UHPC rib, as well as the improved contact area between the UHPC rib and the slab. This leads to an increase in the ultimate load of the structure, reducing the probability of cracks appearing.

The ability of LS-DYNA to accurately capture and record the crack pattern is indicative of its effectiveness in simulating structural behavior under different loading conditions.

6.7. Discussion

This study used a parametric analysis to investigate a range of UHPC compressive strengths ranging from 60 MPa to 180 MPa and conventional concrete strengths ranging from 20 MPa to 40 MPa. Additionally, it investigated the yield strengths of rebars within the range of 387 MPa to 659 MPa. The study involved predicting peak load and crack failures in the UHPC rib, slab, and PC wall, both internally and externally. The findings indicated that enhancing the concrete strength of the UHPC rib and PC wall, as well as the yield strength of the reinforcement, resulted in improved peak load performance. However, the differences in the results were relatively minor. Notably, the shape of the UHPC rib remained constant throughout the analysis. As a result, the concrete strength of the UHPC rib can be modified as needed for practical building applications.

7. Conclusions

The new connections for the UHPC rib and PC wall in the building were developed to improve structural performance compared to the conventional solution. The purpose of this study was to investigate the effect of thermal bridge solutions with one or two shear keys and compare their impact on the bearing capacity of a structure. This comparison was intended to provide a better understanding of the differences in the performance of the solutions. Several of the main conclusions are as follows:

- According to the findings, using high-quality concrete for the UHPC rib has little effect on the overall performance of the structure. As the slab thickness and the number of shear keys increased, the ultimate load increased significantly, by 54.45% and 56.85% respectively. These changes significantly enhanced the structure's bearing capacity.
- A parametric study investigated that increasing the concrete strength of the UHPC rib and PC wall, as well as the yield strength of the reinforcement, led to improved ultimate load results. However, the differences in the results were relatively minor. In addition, the shape of the UHPC rib remained unchanged throughout the analysis. Therefore, the design of the UHPC rib's concrete strength can be adjusted as appropriate for practical building. Based on the survey results, the key parameter identified

Table A.9
Abbreviations used.

Abbreviation	Definition
MAT020	*MAT_RIGID_(020)
MAT03	*MAT_PLASTIC_KINEMATIC_(003)
Winfrith model	*MAT_WINFRITH_CONCRETE_(084/085)
Surface-To-Surface	*CONTACT_AUTOMATIC_SURFACE_TO_SURFACE
Lagrange-In-Solid	*CONSTRAINED_LAGRANGE_IN_SOLID

Table A.10
Results of parametric study obtained from LS-DYNA.

No.	Model	Strength concrete (MPa)		Peak load (kN)	Displacement (mm)	Yield str. (MPa)
		UHPC rib	PC wall			
1	H150-F	160	20	25.7	86.5	502
2		160	25	26.7	66.2	502
3		160	35	27.8	187	502
4		160	40	28.4	73.3	502
5		60	27	23.8	140	502
6		90	27	25.5	109.2	502
7		120	27	27.7	98.9	502
8		180	27	27.9	79.5	502
9		160	27	27.9	160	387
10		160	27	27.3	211	425
11		160	27	29.3	77.9	574
12		160	27	28.3	78.1	659
13		160	27	27.4	60.9	Rate 0
14		160	27	28.12	74.9	Rate 1
15	H210-S	160	20	496	20.4	502
16		160	25	510	21.1	502
17		160	35	525	21.2	502
18		160	40	532	21.6	502
19		60	27	412	21.9	502
20		90	27	460	20.6	502
21		120	27	487	22.4	502
22		180	27	522	22.5	502
23		160	27	507	22.7	387
24		160	27	503	21.7	425
25		160	27	513	20.7	574
26		160	27	536	19.7	659
27		160	27	369	20.6	Rate 1
28		160	27	721	34.6	Rate 2

is the geometric size, which results in a significant variance in the ultimate load. It can be employed to optimize the shape of specimens for research purposes and practical applications.

- The results of the numerical model demonstrated that LS-DYNA could accurately simulate and predict the failure behavior of structures. The model successfully predicted load capacity, with the greatest discrepancy in strength of 6.92% between the model and experimental results. The predicted load-displacement curves were found to closely match the measured response.

However, this study has some limitations. Because four thermal bridge systems were examined, the results cannot be generalized to different structure specifications. In future studies, the thermal and structural performance of thermal bridge solutions in residential buildings will be investigated simultaneously as well in various situations.

CRediT authorship contribution statement

Nguyen Huu Cuong: Writing – review & editing, Writing – original draft, Validation, Software, Methodology, Investigation, Conceptualization. **Hyoseo An:** Writing – review & editing, Investigation. **Han V. Tran:** Validation, Methodology, Data curation. **Sanghee An:** Writing – review & editing, Software, Formal analysis. **Kihak Lee:** Writing – review & editing, Supervision, Resources, Project administration, Formal analysis.

Declaration of competing interest

The authors declare that they have no known competing financial interests or personal relationships that could have appeared to influence the work reported in this paper.

Data availability

The authors do not have permission to share data.

Acknowledgments

This work is supported by the Korea Agency for Infrastructure Technology Advancement (KAIA) grant funded by the Ministry of Land, Infrastructure, and Transport, South Korea (Grant: RS-2020-KA155780).

Appendix A. Results of parametric studies obtained from LS-DYNA

See Tables A.9 and A.10.

Appendix B. Crack and failure of numerical models

See Figs. B.22–B.24.

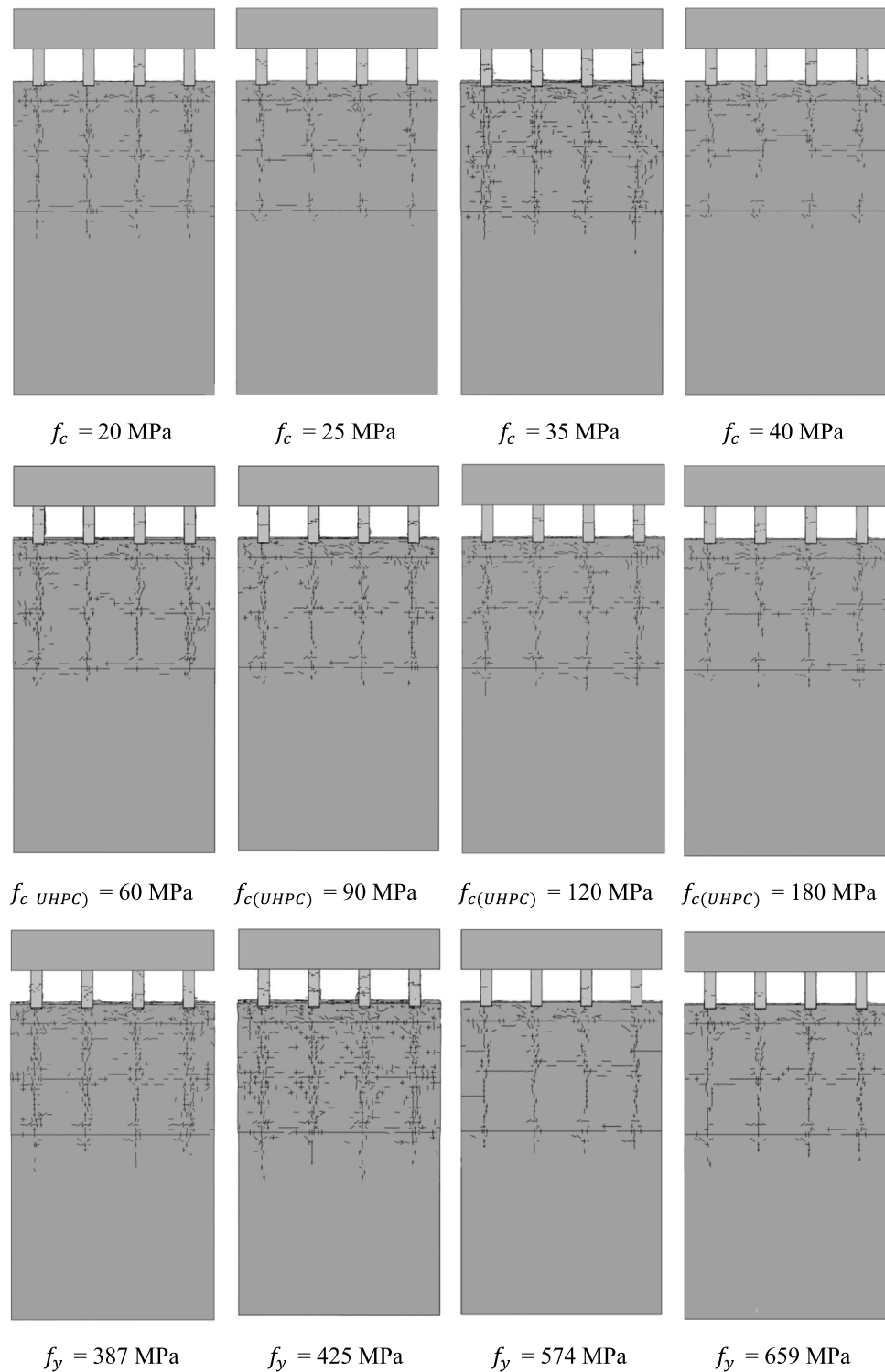


Fig. B.22. Cracks pattern of H150-F numerical models (top).

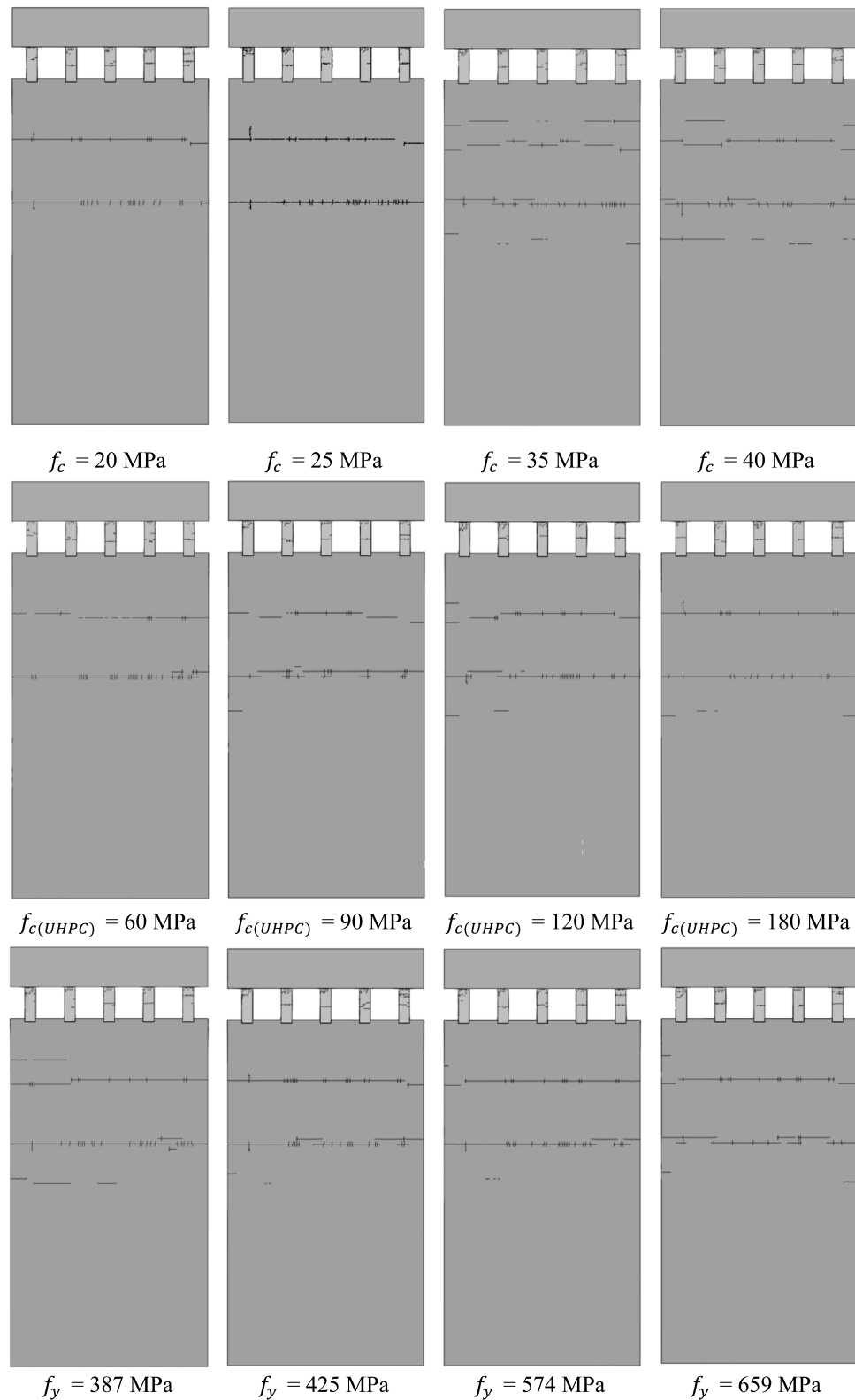


Fig. B.23. Cracks pattern of H210-S numerical models (bottom).

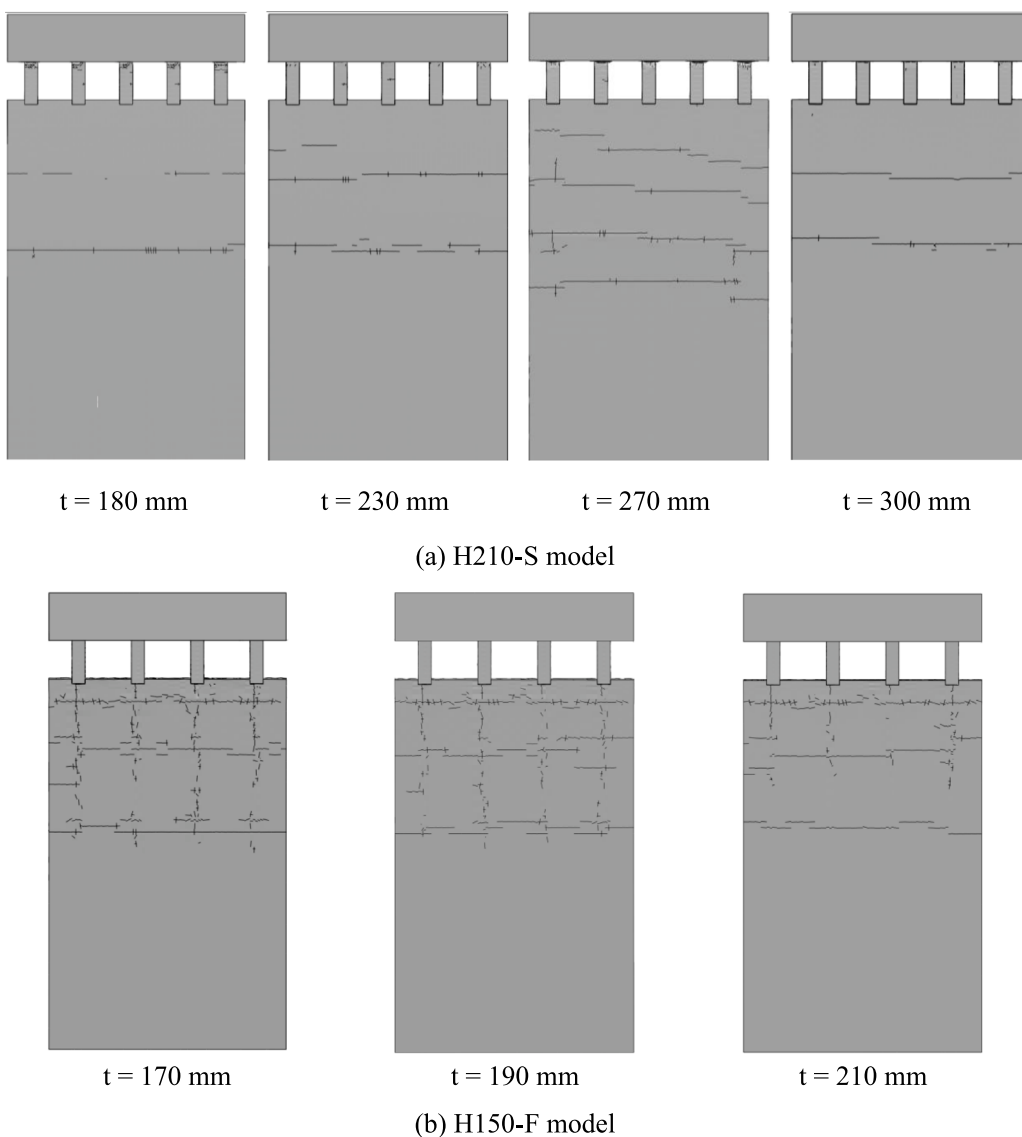


Fig. B.24. Cracks pattern with change in geometry.

References

- [1] Republic of Korea, 2023, Republic of korea, Ministry of Land, Infrastructure and Transport, 2023, <https://www.molit.go.kr/english>.
- [2] H. Ge, V.R. McClung, S. Zhang, Impact of balcony thermal bridges on the overall thermal performance of multi-unit residential buildings: A case study, Energy Build. 60 (2013) 163–173, <http://dx.doi.org/10.1016/J.ENBUILD.2013.01.004>.
- [3] T.G. Theodosiou, A.M. Papadopoulos, The impact of thermal bridges on the energy demand of buildings with double brick wall constructions, Energy Build. 40 (11) (2008) 2083–2089, <http://dx.doi.org/10.1016/J.ENBUILD.2008.06.006>.
- [4] T. Keller, F. Riebel, A. Zhou, Multifunctional all-GFRP joint for concrete slab structures, Constr. Build. Mater. 21 (6) (2007) 1206–1217, <http://dx.doi.org/10.1016/J.CONBUILDMAT.2006.06.003>.
- [5] Z. Wang, K. Maekawa, Lifetime assessment of structural concrete – multi-scale integrated hydro-thermal-chemo-electrical-mechanistic approach and statistical evaluation, Struct. Infrastruct. Eng. 18 (7) (2022) 933–949, <http://dx.doi.org/10.1080/15732479.2021.1995443>.
- [6] F. Riebel, T. Keller, Structural behavior of multifunctional GFRP joints for concrete structures, Constr. Build. Mater. 23 (4) (2009) 1620–1627, <http://dx.doi.org/10.1016/J.CONBUILDMAT.2008.05.013>.
- [7] S. Aghasizadeh, B.M. Kari, R. Fayaz, Thermal performance of balcony thermal bridge solutions in reinforced concrete and steel frame structures, J. Build. Eng. 48 (2022) 103984, <http://dx.doi.org/10.1016/J.JBEME.2021.103984>.
- [8] JeongYangSG, Thermal break solutions, 2023, Republic of Korea, 2023, <https://lbnmodular.com/>.
- [9] K. Dikarev, A. Berezyuk, O. Kuzmenko, A. Skokova, Experimental and numerical thermal analysis of joint connection floor slab balcony slab with integrated thermal break, Energy Procedia 85 (2016) 184–192, <http://dx.doi.org/10.1016/j.egypro.2015.12.325>.
- [10] K. Ghazi Wakili, H. Simmler, T. Frank, Experimental and numerical thermal analysis of a balcony board with integrated glass fibre reinforced polymer GFRP elements, Energy Build. 39 (1) (2007) 76–81, <http://dx.doi.org/10.1016/J.ENBUILD.2006.05.002>.
- [11] C. Murad, H. Doshi, R. Ramakrishnan, Impact of insulated concrete curb on concrete balcony slab, Procedia Eng. 118 (2015) 1030–1037, <http://dx.doi.org/10.1016/J.PROENG.2015.08.545>.
- [12] H. Ge, F. Baba, Dynamic effect of thermal bridges on the energy performance of a low-rise residential building, Energy Build. 105 (2015) 106–118, <http://dx.doi.org/10.1016/J.ENBUILD.2015.07.023>.
- [13] K. Goulouti, J. De Castro, A.P. Vassilopoulos, T. Keller, Thermal performance evaluation of fiber-reinforced polymer thermal breaks for balcony connections, Energy Build. 70 (2014) 365–371, <http://dx.doi.org/10.1016/J.ENBUILD.2013.11.070>.
- [14] V. Kodur, S. Banerji, R. Solhmirzaei, Effect of temperature on thermal properties of ultrahigh-performance concrete, J. Mater. Civ. Eng. 32 (8) (2020) 04020210, [http://dx.doi.org/10.1061/\(ASCE\)MT.1943-5533.0003286](http://dx.doi.org/10.1061/(ASCE)MT.1943-5533.0003286).
- [15] M. Abid, X. Hou, W. Zheng, R.R. Hussain, High temperature and residual properties of reactive powder concrete – A review, Constr. Build. Mater. 147 (2017) 339–351, <http://dx.doi.org/10.1016/J.CONBUILDMAT.2017.04.083>.
- [16] H. Yin, K. Shirai, W. Teo, Numerical model for predicting the structural response of composite UHPC-concrete members considering the bond strength at the interface, Compos. Struct. 215 (2019) 185–197, <http://dx.doi.org/10.1016/J.COMPSTRUCT.2019.02.040>.

- [17] S. Epackachi, A.S. Whittaker, A validated numerical model for predicting the in-plane seismic response of lightly reinforced, low-aspect ratio reinforced concrete shear walls, Eng. Struct. 168 (2018) 589–611, <http://dx.doi.org/10.1016/J.ENGSTRUCT.2018.04.025>.
- [18] D.K. Thai, D.L. Nguyen, T.H. Pham, Q.H. Doan, Prediction of residual strength of FRC columns under blast loading using the FEM method and regression approach, Constr. Build. Mater. 276 (2021) <http://dx.doi.org/10.1016/J.CONBUILDMAT.2021.122253>.
- [19] M. Asgarpoor, A. Gharavi, S. Epackachi, Investigation of various concrete materials to simulate seismic response of RC structures, Structures 29 (2021) 1322–1351, <http://dx.doi.org/10.1016/J.STRUCTURE.2020.11.042>.
- [20] S. Azad, S.R. Mirghaderi, S. Epackachi, Numerical investigation of steel and composite beam-to-encased composite column connection via a through-plate, Structures 31 (2021) 14–28, <http://dx.doi.org/10.1016/J.JSTRU.2021.01.040>.
- [21] N. Hagh, S. Epackachi, M. Taghi Kazemi, Cyclic performance of composite shear walls with boundary elements, Structures 27 (2020) 102–117, <http://dx.doi.org/10.1016/J.JSTRU.2020.05.020>.
- [22] C. ASTM, 39/C 39M: The American society for testing materials, 2001, Standard Test Method for Compressive Strength of Cylindrical Concrete Specimens, West Conshohocken (PA), USA.
- [23] B.A. Graybeal, Compression testing of ultra-high-performance concrete, Adv. Civ. Eng. Mater. 4 (2) (2015) 102–112, <http://dx.doi.org/10.1520/ACEM20140027>.
- [24] C1856/C1856M-17 ASTM, Standard Practice for Fabricating and Testing Specimens of Ultra-High Performance Concrete, ASTM International, West Conshohocken, PA, 2017.
- [25] Q.B. To, J. Shin, G. Lee, H. An, K. Lee, Experimental assessment and effective bond length for RC columns strengthened with aramid FRP sheets under cyclic loading, Eng. Struct. 294 (2023) 116642, <http://dx.doi.org/10.1016/j.engstruct.2023.116642>.
- [26] M. Hu, Q. Han, S. Wu, X. Du, Shear capacity of precast concrete shear keys with ultrahigh-performance concrete for connections, J. Bridge Eng. 26 (7) (2021) 04021036, [http://dx.doi.org/10.1061/\(ASCE\)BE.1943-5592.0001734](http://dx.doi.org/10.1061/(ASCE)BE.1943-5592.0001734).
- [27] B.A. Gopal, F. Hejazi, M. Hafezolghorani, V. Yen Lei, Numerical analysis and experimental testing of ultra-high performance fibre reinforced concrete keyed dry and epoxy joints in precast segmental bridge girders, Int. J. Adv. Struct. Eng. 11 (4) (2019) 463–472, <http://dx.doi.org/10.1007/S40091-019-00246-6/FIGURES/7>.
- [28] V. Promotionsausschuss, Ultra-high performance concrete (UHPC) precast segmental bridges-flexural behaviour and joint design, 2016.
- [29] T. Shi, X. Zhang, H. Hao, G. Xie, Experimental and numerical studies of the shear resistance capacities of interlocking blocks, J. Build. Eng. 44 (2021) 103230, <http://dx.doi.org/10.1016/J.JB.2021.103230>.
- [30] G. Rombach, A. Specker, Design of joints in segmental hollow box girder bridges, 2002.
- [31] JSCE, Standard specifications for concrete structures, 2007, design Japan society of civil engineers, 2007, JSCE guidelines for Concrete.
- [32] M.A. Issa, H.A. Abdalla, Structural behavior of single key joints in precast concrete segmental bridges, J. Bridge Eng. 12 (3) (2007) 315–324, [http://dx.doi.org/10.1061/\(ASCE\)1084-0702\(2007\)12:3\(315\)](http://dx.doi.org/10.1061/(ASCE)1084-0702(2007)12:3(315)).
- [33] K. Yoshio, J.C. Jerome, C.T. Thanasis, K.L. Christopher, Fracture mechanics approach for failure of concrete shear key. I: Theory, J. Eng. Mech. 119 (4) (1993) 681–700, [http://dx.doi.org/10.1061/\(ASCE\)0733-9399\(1993\)119:4\(681\)](http://dx.doi.org/10.1061/(ASCE)0733-9399(1993)119:4(681)).
- [34] K. Yoshio, J.C. Jerome, C.T. Thanasis, K.L. Christopher, Fracture mechanics approach for failure of concrete shear key. II: Verification, J. Eng. Mech. 119 (4) (1993) 701–719, [http://dx.doi.org/10.1061/\(ASCE\)0733-9399\(1993\)119:4\(701\)](http://dx.doi.org/10.1061/(ASCE)0733-9399(1993)119:4(701)).
- [35] W. Hou, M. Peng, B. Jin, Y. Tao, W. Guo, L. Zhou, Influencing factors and shear capacity formula of single-keyed dry joints in segmental precast bridges under direct shear loading, Appl. Sci. 10 (18) (2020) 6304, <http://dx.doi.org/10.3390/APP10186304>.
- [36] M. Hu, Z. Jia, Q. Han, Y. Ni, C. Jiao, P. Long, Shear behavior of innovative high performance joints for precast concrete deck panels, Eng. Struct. 261 (2022) 114307, <http://dx.doi.org/10.1016/J.ENGSTRUCT.2022.114307>.
- [37] N.-V. Luat, J. Shin, J.-H. Park, K. Lee, Experimental and numerical investigation on seismic performance of retrofitted RC columns with web direct/indirect bonding external H-section, J. Build. Eng. 44 (July) (2021) 103404, <http://dx.doi.org/10.1016/j.jobe.2021.103404>.
- [38] G. Tunc, M.M. Othman, H.C. Mertol, Finite element analysis of frames with reinforced concrete encased steel composite columns, Buildings 12 (3) (2022) 375, <http://dx.doi.org/10.3390/BUILDINGS12030375>.
- [39] S. Xu, B. Chen, Q. Li, F. Zhou, X. Yin, X. Jiang, P. Wu, Experimental and numerical investigations on ultra-high toughness cementitious composite slabs subjected to close-in blast loadings, Cem. Concr. Compos. 126 (2022) 104339, <http://dx.doi.org/10.1016/J.CEMCONCOMP.2021.104339>.
- [40] S. Sengel, H. Erol, T. Yilmaz, Ö. Anil, Investigation of the effects of impactor geometry on impact behavior of reinforced concrete slabs, Eng. Struct. 263 (2022) 114429, <http://dx.doi.org/10.1016/J.ENGSTRUCT.2022.114429>.
- [41] A. Selim Sengel, Low-velocity impact behavior of two-way RC slab strengthening with carbon TRM strips, Structures 44 (2022) 1695–1714, <http://dx.doi.org/10.1016/J.JSTRU.2022.08.108>.
- [42] E. Owen, Webinar: LS-DYNA introduction to contacts, 2020.
- [43] M. Abedini, C. Zhang, Performance assessment of concrete and steel material models in LS-DYNA for enhanced numerical simulation, A state of the art review, Arch. Comput. Methods Eng. 28 (4) (2021) 2921–2942, <http://dx.doi.org/10.1007/S11831-020-09483-5/METRICS>.
- [44] F.H. Wittmann, K. Rokugo, E. Brühwiler, H. Mihashi, P. Simonin, Fracture energy and strain softening of concrete as determined by means of compact tension specimens, Mater. Struct. 21 (1) (1988) 21–32, <http://dx.doi.org/10.1007/BF02472525>.
- [45] M.Z. Zhao, D.E. Lehman, C.W. Roeder, Modeling recommendations for RC and CFST sections in LS-Dyna including bond slip, Eng. Struct. 229 (2021) 111612, <http://dx.doi.org/10.1016/J.ENGSTRUCT.2020.111612>.